Key Points:

- Paleoseismology based on identification of turbidites and homogenites along the Lesser Antilles subduction zone
- Several megathrust earthquakes have been highlighted over the last 120 Kyrs offshore Guadeloupe
- Four major earthquakes triggered up to 8 m-thick homogenite deposits

Correspondence to:

C. Seibert,
cseibert@ldeo.columbia.edu

Sedimentary Records in the Lesser Antilles Fore-Arc Basins Provide Evidence of Large Late Quaternary Megathrust Earthquakes

C. Seibert[1,2] , N. Feuillet[1], G. Ratzov[3], C. Beck[4], P. Morena[3,5,6] , L. Johannes[7], E. Ducassou[8], A. Cattaneo[5], C. Goldfinger[9], E. Moreno[10] , A. Bieber[1,11], G. Bénâtre[1], B. Caron[12], M. Caron[11] , M. Casse[11], T. Cavailhes[8], G. Del Manzo[1] , C. E. Deschamps[11] , P. A. Desiage[11] , Q. Duboc[11], K. Fauquembergue[8] , A. Ferrant[13], H. Guyard[1], E. Jacques[1], M. Laurencin[14] , F. Leclerc[3] , J. Patton[9] , J. M. Saurel[1], G. St-Onge[11], and P. Woerther[13]

[1]Université de Paris Cité, Institut de Physique du Globe de Paris, CNRS, Paris, France, [2]Lamont-Doherty Earth Observatory of Columbia University, Palisades, NY, USA, [3]Université Côte d'Azur, CNRS, IRD, Observatoire de la Côte d'Azur, Géoazur, Nice, France, [4]ISTerre, CNRS, Université Savoie-Mont-Blanc, Le Bourget du Lac, France, [5]IFREMER, Geo-Ocean, UMR6538, Plouzané, France, [6]Université de Brest, LGO UMR 6538, Plouzané, France, [7]Muséum National d'Histoire Naturelle, UMR 7207, Département Histoire de la Terre, Paris, France, [8]Université de Bordeaux, UMR CNRS 5805 EPOC, Pessac, France, [9]College of Earth, Ocean, and Atmospheric Sciences, Oregon State University, Corvallis, OR, USA, [10]Laboratoire d'Océanographie et du Climat (LOCEAN), Sorbonne Université/CNRS/IRD/MNHN, Paris, France, [11]Institut des sciences de la mer de Rimouski (ISMER), Canada Research Chair in Marine Geology, Université du Québec à Rimouski (UQAR) and GEOTOP, Rimouski, QC, Canada, [12]Sorbonne Université, CNRS-INSU, Institut des Sciences de la Terre de Paris, ISTeP UMR 7193, Paris, France, [13]Unité Recherche et Développements Technologiques, Ifremer, Plouzané, France, [14]Laboratoire d'Océanologie et Géosciences, Université de Lille, Villeneuve d'Ascq, France

Abstract The seismic potential of the Lesser Antilles subduction zone is poorly known and highly debated. Only two damaging earthquakes have been reported in the historical period, in 1839 and 1843, but their sources and magnitude are still uncertain. Global Navigation Satellite Systems and coral data contradict each other, and no conclusion has been reached on the coupling ratio of the plate interface. Given the threat posed by the possible occurrence of a large megathrust earthquake, it is crucial to gain information on prehistorical events. We present the results of a submarine paleoseismological study that covers an exceptional ~120 Kyr-long period. We studied the sediments sampled in six up to 26 m-long piston cores collected in deep fore-arc basins located over the epicentral region of the 1843 earthquake. Using a multiproxy approach combining geophysical, geochemical, and sedimentological analysis, biostratigraphy and radiocarbon dating, we identified, characterized, and dated numerous event deposits that we then correlated with the sampled basins over an up to 160 km-long area. We show that at least 33 earthquakes likely triggered these sediment remobilizations in the last 120 Kyr. Four of these events promoted exceptional deposits of turbidites + homogenites. From peak ground acceleration calculated for potential earthquakes occurring on various faults, and the absence of deposits linked to the historical earthquakes, we propose that the sources are likely megathrust earthquakes. Over the last 60 Kyr, we inferred at least three 15–25 Kyr-long seismic cycles in which the recurrence times of earthquakes shortens from ~5 to ~2 Kyr.

1. Introduction

Along subduction zones, high-magnitude megathrust earthquakes, such as those having occurred offshore Sumatra in 2004 (Mw 9.3, Lay et al., 2005), Chile in 2010 (Mw 8.8, Tong et al., 2010) and northern Japan in 2011 (Mw 9.1, Ammon et al., 2011) may only repeat with time intervals of several centuries or millennia (Goldfinger et al., 2003; Minoura et al., 2001; Sieh et al., 2008). They can be highly destructive and are often associated with devastating tsunamis. They thus threaten vast coastal zones, often with increasing population densities. Existing models of seismic cycles failed to anticipate those exceptional events, and in most areas, the instrumental and historical records are too short to document the long-term behavior of subduction zones.

Getting long-term records of earthquakes by collecting paleoseismological information in the geological record, both onshore and offshore, is currently the only way to better constrain the catalog of large earthquakes in an area. Offshore, major earthquakes and associated tsunamis can trigger submarine slope failures, mass-wasting, remobilize the surficial sediment over large areas, which can be further identified as an event deposit (mass transport

deposit, turbidite, homogenite…) disrupting the continuous long-term sedimentation record (Beck et al., 2012; Heezen & Ewing, 1952; McHugh et al., 2016; Mountjoy et al., 2018). Over the last decades, numerous studies based on the identification of earthquake-triggered sediment deposits have brought crucial results to constrain the seismic behavior of actively deforming zones worldwide, within areas affected by crustal and local faults (Babonneau et al., 2017; Beck, 2009; Beck et al., 2012; Grácia et al., 2010; Ratzov et al., 2015), and at subduction zones (Adams, 1990; Goldfinger et al., 2003, 2012; Nakajima & Kanai, 2000; Patton et al., 2013, 2015; Pouderoux et al., 2012, 2014; Usami et al., 2018). However, only a few studies show records longer than the Holocene (Pouderoux et al., 2014). Recently, Usami et al. (2018) documented that along the Japan trench, only great (Mw ~ 8) and giant (Mw ~ 8.5–9) earthquakes having ruptured a large part of the plate interface can promote turbidity currents. The use of turbidites as paleo-earthquake proxies remains challenging because gravity flows can be triggered by other processes such as flood-driven hyperpycnal flows, volcanic eruptions, sediment loads, tsunami or storm wave loading, or bolide impacts (Goldfinger et al., 2012; Normark & Piper, 1991; Talling, 2014).

To distinguish between earthquake-triggered sediment deposits and other deposits, two main strategies can be applied: one consists of searching for synchronous deposition of event deposits over independent sedimentary systems in the fore-arc (basins, canyons, channels, or the trench), and the second focuses more on a detailed sedimentary analysis of the event deposits to trace back the triggering, transport and depositional mechanisms (i.e., Beck et al., 2007, 2012; Goldfinger et al., 2012; Migeon et al., 2017; Nakajima & Kanai, 2000; Van Daele et al., 2017). A good strategy is to target sites isolated from terrestrial sediment sources in which only localized self-failures and earthquakes of various types can trigger turbidity currents (Patton et al., 2015). We applied those methods to better constrain the seismic potential of the Lesser Antilles subduction zone.

We present the results of a multiproxy study of exceptional long-term sedimentary records, from six to 26 m-long giant piston cores, collected in the fore-arc basins of the Lesser Antilles arc during the CASEIS cruise between 28th May and 05th July 2016 on board of the R/V *Pourquoi Pas*? (Feuillet, 2016). We combined geophysical, geochemical and sedimentological data to identify instantaneous sedimentary deposits triggered by earthquakes (mass transport deposits, turbidites, and homogenites). We establish their chronology and elaborate a long-term paleoseismic record covering the late Quaternary. We then discuss the sources and possible size of earthquake ruptures and possible fault-rupture segmentation of the Lesser Antilles plate interface. Based on our hypothesis concerning the sources of earthquakes and the chronology of the main seismic events, we provide constraints on the long-term seismological behavior of the Lesser Antilles megathrust.

2. Geological Setting

2.1. Tectonic Setting and Seismicity

The Lesser Antilles arc results from the subduction of the North and South American plates beneath the Caribbean plate at rates of about 2 cm/yr along an ENE-WSW direction (DeMets et al., 2000; Symithe et al., 2015). It is 850 km long extending from the Venezuelan coasts to the Virgin Islands and made of two subparallel volcanic ridges in the northern portion that splay from Martinique, and are separated by the Kallinago Trough (Bouysse & Westercamp, 1990) (Figure 1a). The western ridge is made of volcanic islands (inner arc, Volcanic Caribbees) on which lie the recent Plio-Quaternary and active volcanic systems. The eastern ridge is made of an older Paleogene volcanic system now extinct, abraded and capped by Neogene carbonate platforms (Limestone Caribbees). The division of the arc was inferred to be the result of a major reorganization of the subduction following the entry of the non-buoyant Barracuda and Tiburon ridges in the system (Bouysse & Westercamp, 1990; Pichot et al., 2012).

The seismic behavior of the Lesser Antilles megathrust is poorly known and still highly debated. No megathrust earthquake comparable to the 2004 Sumatra or 2011 Tohoku earthquakes has been reported in the historical earthquake catalog. This catalog is however very short, beginning only in the middle of the 17th century. There is a strong debate on the coupling ratio of the plate interface: although the modeling of the Caribbean upper plate surface short-term geodetic deformations suggests a low coupling ratio of the megathrust (meaning that no significant slip deficit is accumulating that could be released in a future large earthquake at the plate interface, Manaker et al., 2008; Symithe et al., 2015; van Rijsingen et al., 2021), that of longer term coral microatoll behavior (over decades and centuries) indicates a strong coupling (Philibosian et al., 2022; Weil-Accardo et al., 2016). The recent discovery of prehistorical tsunami deposits along the coasts of northern Lesser Antilles islands also suggests potential megathrust earthquake activity in the region (Biguenet et al., 2021, 2022; Cordrie et al., 2022).
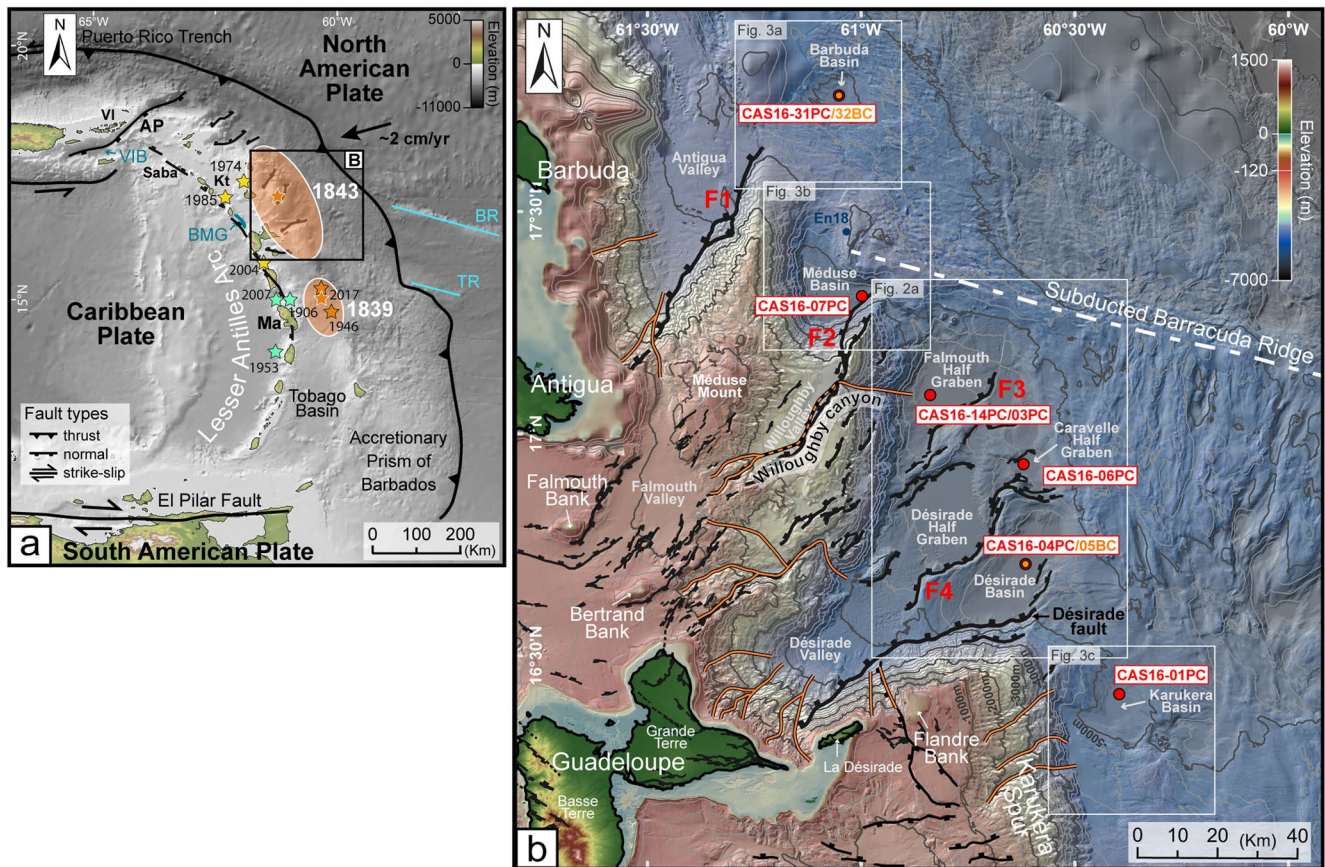
Figure 1. Lesser Antilles arc geodynamic setting and the "Rough" area. (a) Regional map of the Lesser Antilles arc showing the geodynamic context, black arrow: convergence rate (DeMets et al., 2000), light blue lines: Barracuda Ridge (BR) and the Tiburon Ridge (TR), VIB: Virgin Island Basin, VI: Virgin Islands, BMG: Bouillante-Montserrat graben, AP: Anegada Passage, Ma: Martinique, Kt: Kallinago trough. Stars: earthquake location, on crustal fault (yellow stars), subducting slab (green stars) and subduction interface (orange stars). Orange ellipses: inferred rupture areas of the earthquake of 11 January 1839 and the earthquake of 8 February 1843 (Feuillet et al., 2011). (b) Rough eastern area map (located on A) with the location of the sedimentary cores (red dots for the piston cores and orange dots for the interface box-cores). Bathymetry: high-resolution multibeam data from numerous marine cruises (see Seibert et al., 2020) gathered in a GIS database. The fault mapping (black lines) comes from Feuillet et al. (2001). Orange lines: major canyons (from Seibert et al. (2020); for more detail refer to this publication), white dotted line: subducted part of Barracuda Ridge; Blue dot: location of the En18 core analyzed by Reid et al. (1996); dark gray isobaths every 1,000 m, and light gray isobaths every 250 m.

Although the seismicity rate in the Lesser Antilles subduction zone is low compared to other subduction zones, numerous earthquakes have been recorded and documented during the historical and instrumental periods (Bernard & Lambert, 1988; Dorel, 1981; Feuillard, 1985; Feuillet et al., 2011; Robson, 1964; Stein et al., 1982; Sykes & Ewing, 1965). The two largest historical earthquakes occurred 4 years apart on 11th January 1839 and on 8th February 1843 (Figure 1a; Feuillet et al., 2011). The 1843 earthquake, the strongest (intensity up to X), destroyed the main city of Guadeloupe (Dorel, 1981; Feuillard, 1985; Sainte-Claire Deville, 1843), killing more than 1,500 people. It was felt with an intensity II along the east coast of the United States (Hough, 2013). Historical reports in Guadeloupe and Antigua suggest that it was followed by a ~1 m high tsunami wave (Sainte-Claire Deville, 1843; Shepherd, 1992). There are still large uncertainties on the magnitude of this event: whereas Bernard and Lambert (1988) inferred a magnitude of 7.5, Robson (1964), Feuillet et al. (2011), and Hough (2013) estimated magnitudes up to 8.5. The sources of both the 1839 and 1843 earthquakes remain unconstrained. The most recent studies inferred that those earthquakes ruptured deep portions of the plate interface (Feuillet et al., 2011). The seismic activity of the area is also characterized by moderate magnitude 6-7-class earthquakes that ruptured either shallow crustal faults in the overriding plate (M7.4 8th October 1974, M6.3 16th March 1985 and Mw6.3 21st November 2004 earthquakes, Figure 1a) or deep (100–150 km) portions of the subducting slab (16th February 1906, M7-7.5 19th March 1953, M7.4 29th November 2007, Figure 1a; Bazin et al., 2010; Feuillard, 1985; Feuillet et al., 2011; Ruiz et al., 2013; Stein

et al., 1982 and references therein). The crustal shallow earthquakes occur on two sets of active normal faults that accommodate the oblique convergence between the North American and the Caribbean plates (Feuillet et al., 2002, 2004, 2010; Leclerc et al., 2016): (a) A NE-SW striking system in the fore-arc domain that forms graben and half graben perpendicular to the arc between the Virgin Islands and the Guadeloupe island and (b) an arc-parallel en-échelon fault system between Saba and Martinique (Figure 1). Crustal active faulting, megathrust earthquakes, the subduction of the Barracuda and Tiburon ridges (Figure 1a), the growth of the accretionary wedge, the development of reef platforms and the volcanic processes shape the seafloor morphology at various space and time scales (Boucard et al., 2021; Feuillet et al., 2002, 2010, 2011; Laigle et al., 2013; Laurencin et al., 2019; Macintyre, 1972) and exert a control on the sedimentary processes (Morena et al., 2022; Seibert et al., 2020). As expected in a mixed carbonated-siliciclastic environment along an active margin where large earthquakes, tsunamis, volcanic events and hurricanes can occur, the sediments that were cored in the Lesser Antilles in the framework of previous investigations are diverse: tephra falls, deposits from reef platform or volcanic flank instabilities, turbidites of various nature (Beck et al., 2012; Bieber et al., 2021; Brunet et al., 2016; Le Friant et al., 2008; Morena et al., 2022; Picard et al., 2006; Reid et al., 1996; Seibert et al., 2020; Trofimovs et al., 2013).

2.2. Sampling Site

The sampling area is located in the fore-arc domain, above the megathrust in the epicentral area of the 1843 earthquake in between the steep slopes of the Lesser Antilles arc and the accretionary wedge (Figure 1a). The morphology of this area was described in detail by Seibert et al. (2020) and we summarize here the key points. In this area, the seafloor is disrupted and shaped by N50°E to E-W striking normal faults and tilted blocks with a thousand meters high scarps and steep slopes bounding up to 5,800 m deep basins (Figure 1b). The slopes are incised by numerous submarine canyons, likely as a result of regressive erosion. Most are straight and short, restricted to the steepest slopes. Others (Willoughby canyon, Figure 1b) are longer, flowing in flatter half-grabens at the base of active faults, which thus control the turbiditic systems. Some canyons are located upstream of U-shaped valleys (Antigua, Désirade) and their heads incise the edges of the Guadeloupean and Antiguan insular shelf. Those canyons are thus likely able to transfer sediments from shallow environments to deeper zones of the area. Others, originating from deeper areas in between islands (Karukera Spur, Falmouth Valley, Méduse Mount) are completely disconnected from the insular shelves and carbonate platform and flow in basins isolated from one another by high structural reliefs. As a consequence, several basins in the area (the ~5,830 m below sea level—mbsl—Falmouth Half Graben, the ~5,200 mbsl Karukera Basin and the ~5,500 mbsl Méduse Basin) are completely isolated from the sediment supply of shallow environments. They are likely fed only by sediments accumulated on the slopes and carried either by slope-confined canyons or by landsliding (Seibert et al., 2020). The ~5,590 mbsl Caravelle Half Graben and the ~5,100 mbsl Barbuda Basin are located upstream of the U-shaped Antigua and Désirade valley but are isolated from the margin by several hundred-meter normal fault scarps and by structures of the accretionary wedge.

We collected the cores in those fore-arc basins (Figure 1b) out of which all but one (the ~5,710 mbsl Désirade Basin) are ideal targets for paleoseismological investigations (Seibert et al., 2020). They are disconnected from terrestrial sources, far from the volcanic system and distributed over a wide area. In those basins, we expected to sample only seismically generated event deposits, avoiding those triggered by other processes such as storm wave loading at shallow water depths, volcanic flank instabilities, density cascading, hyperpycnal flow and local slope failures. The Falmouth Half Graben, Caravelle Half Graben and the Désirade Basin are part of the Désirade Trough sub-basins (Figure 1b). The northernmost sampled core (core CAS16-31PC) was collected in the Barbuda Basin, northward to the Barracuda ridge that is a major subducting relief in the area (Pichot et al., 2012). Trace is clearly visible in the accretionary wedge as N110°E oriented relief, with its north-western tip controlling the morphology of the Méduse Basin, as it steepens the basin's north-eastern slope creating high relief (Figure 1b). On this relief, one core (En18, Figure 1b) was sampled in our site area in the seventies and further analyzed by Reid et al. (1996). These authors have shown that the background sedimentation consists of pelagic carbonate or pelagic clay minerals. They observed that the volcanoclastic particles of the sediments represent less than 10% (mostly in tephra fallouts), the shallow-water carbonate from the platforms around 5%, and rare event deposits (<1 layer/m), which interrupt the background sedimentation. Low sedimentation rates (between 1 and 3 cm/Kyr) were determined in the area in agreement with those estimated more recently offshore Martinique (Bieber et al., 2021) in a comparable structural context. Higher sedimentation rates were estimated in fore-arc basins

Table 1
Location and Characteristics of the Sediment Cores of This Study

Cores	Latitude	Longitude	Water depth (m)	Cores' length (m)
CAS16-01PC	16°24.576′N	60°23.648′W	5,203	9
CAS16-03PC	17°05.218′N	60°50.252′W	5,822	9.44
CAS16-04PC	16°42.380′N	60°36.907′W	5,706	19.10
CAS16-05BC	16°42.380′N	60°36.907′W	5,706	0.53
CAS16-06PC	16°55.836′N	60°37.135′W	5,585	19.35
CAS16-07PC	17°18.481′N	60°59.840′W	5,425	19
CAS16-14PC	17°05.212′N	60°50.248′W	5,821	26.45
CAS16-31PC	17°45.642′N	61°03.098′W	5,097	21
CAS16-32BC	17°45.642′N	61°03.098′W	5,097	0.51

(between 5 and 15 cm/Kyr, with higher rates during the most recent glaciation) but farther south or west of Dominica or in the Tobago trough (Reid et al., 1996).

3. Methods

We performed a multidisciplinary and multiproxy paleo-seismological study of the CASEIS data by combining information from geophysical data (bathymetry and sub-bottom profiles—SBP), sedimentological analysis (Multi Core Sensor Logger physical—MSCL—data and photographs, X-ray fluorescence -XRF, chemical measurement, grain-size, biostratigraphy) and ^{14}C dating. The maps presented in this study were prepared with a geographic information system gathering high-resolution multibeam bathymetric and backscatter data acquired during numerous marine cruises, including CASEIS (see Seibert et al., 2020 for details). The SBP data were acquired with an IxBlue ECHOES 3500 T7 with a 4kVA amplifier by using a signal frequency source ranging between 1.8 and 5.3 kHz. The theoretical vertical resolution is about 20 cm and the maximum penetration depth is 150 m in clay at 1,000 m depth (see https://www.ixblue.com/wp-content/uploads/2021/12/echoes-3500-t7.pdf for details).

We studied six 9–26.45 m-long cores collected with a Calypso piston coring system, from South to North: core CAS16-01PC in the Karukera Basin, core CAS16-04PC in the Désirade Basin, core CAS16-06PC in the Caravelle Half Graben, core CAS16-14PC in the Falmouth Half Graben, core CAS16-07PC in the Méduse Basin and core CAS16-31PC in the Barbuda Basin (Table 1; Figure 1b). A second piston core (CAS16-03PC) was collected in the Falmouth Half Graben, shorter than the core CAS16-14PC (9.14 m-long; Table 1; Supplementary S1-1 in Supporting Information S1). We used both cores to better characterize the recent sediment record in this basin. The sampling was complemented by two box-cores (interface cores) in two sites, in the Désirade Basin with core CAS16-05BC and in the Barbuda Basin with core CAS16-32BC (Table 1; Figure 1b; Supplementary S1-2 in Supporting Information S1). This was motivated by the fact that the top of the piston cores may be lost or disturbed by the Calypso corer. The mobile part of the piston corer was equipped with sensors to measure the acceleration and vertical displacement. Those data were analyzed with the software CINEMA developed by IFREMER to evaluate the quality of the coring (Woerther, 2016). They reveal that the sediment/water interface was sampled, thus that the loss of material in the upper part of the core is expected to be limited (a few centimeters). They also show that the upper part of the cores was stretched by 10%–25% over a thickness of 4–6 m for cores CAS16-01PC, CAS16-04PC, CAS16-06PC, CAS16-07PC, and CAS16-31PC and 9 m for CAS16-14PC. We correlated the sediment cores with stationary SBP data resulting from continuous stationary recording during the coring operation.

Onboard, before splitting the cores, we scanned them with the GEOTEK MSCL of the Québec University at Rimouski (UQAR) for P-wave velocity, gamma density, and volumetric magnetic susceptibility (response function with the loop of 12 cm). High-resolution photographs, surface magnetic susceptibility and spectrophotocolorimetry were obtained on split cores with a measurement every cm using the MSCL. After the cruise, we performed several analyses on the cores presented in this study. We used the SCOPIX system (UMR EPOC—Bordeaux) and the GEOTEK X-ray CT (IFREMER—Brest) to obtain X-ray 2D images. Semi-quantitative chemical elementary profiles were measured with an AVAATECH XRF core scanner at UMR EPOC and IFREMER with a pitch of 1 cm at 10 and 30 kV. We plotted different ratios and used scatter plots of different elements for cluster analysis. We collected 44 samples in sandy intervals in core CAS16-14PC (Falmouth Half Graben) and 5 samples in the main gravity deposits of core CAS16-04PC (Désirade Basin) to determine their composition. They were sieved at 63 μm to characterize foraminifera and mineral content under a binocular.

The chronology of event deposits in all cores was obtained using AMS ^{14}C dating on at least 10 mg of planktonic foraminifera picked from the >150 μm sediment fraction a few centimeters below or above turbidites (Table 2) at LMC14 (ARTEMIS CNRS facility, France) or the BETA ANALYTICS Laboratory (USA). The radiocarbon ages were calibrated with the OxCal 4.4 software (Bronk Ramsey, 2009) using the IntCal Marine20 calibration curve (Heaton et al., 2020), and the regional offset ΔR value of -156 ± 32 years, recalculated from Paterne et al. (2018) for the MARINE20 curve (with CALIB REV8.2 software, Stuiver et al., 2021). Then, we used a Bayesian model with a P-sequence deposition model in OxCal (Poisson distribution, Bronk Ramsey, 2008;

Table 2
List of Radiocarbon Ages Sampled in the Cores, Dated Either in LMC Saclay or in the Beta Analytic Laboratory (Beta A.)

Cores	Sample intervals (cm)	Natures of sample	Lab.	Radiocarbon age (BP)	Calibrated age (BP)
CAS16-01PC	18–19	*G. sacculifer*	LMC	**2,635 ± 30**	2,353 ± 98
CAS16-01PC	40–41	*G. sacculifer*	LMC	**6,130 ± 30**	6,527 ± 89
CAS16-01PC	158–159	*G. ruber, G. trilobus, G. sacculifer, G. conglobatus*	Beta A.	**28,720 ± 130**	32,237 ± 273
CAS16-01PC	173–174	*G. ruber*	Beta A.	**28,910 ± 160**	32,484 ± 293
CAS16-01PC	191–192	*G. sacculifer*	LMC	**30,360 ± 320**	34,186 ± 323
CAS16-01PC	264–265	*G. ruber*	Beta A.	**36,540 ± 290**	40,696 ± 256
CAS16-03PC	596–597	*G. trilobus, G. sacculifer*	Beta A.	**7,550 ± 30**	7,987 ± 81
CAS16-04PC	5–6	Bulk	Beta A.	**3,100 ± 30**	2,907 ± 88
CAS16-04PC	113.5–114.5	Bulk	LMC	6,985 ± 30	7,440 ± 73
CAS16-04PC	333–334	*G. trilobus, G. sacculifer*	Beta A.	**7,180 ± 30**	7,617 ± 74
CAS16-04PC	345–346	*G. trilobus, G. sacculifer*	Beta A.	**8,480 ± 30**	9,103 ± 93
CAS16-04PC	357.5–358.5	*G. ruber, G. trilobus, G. sacculifer*	Beta A.	8,380 ± 30	8,959 ± 104
CAS16-04PC	372.5–373.5	*G. trilobus, G. sacculifer*	Beta A.	**9,920 ± 30**	10,982 ± 109
CAS16-04PC	587.5–586.5	*G. sacculifer*	Beta A.	**30,560 ± 170**	34,352 ± 173
CAS16-04PC	919–920	*N. Dutertrei*	LMC	**33,660 ± 470**	37,818 ± 638
CAS16-05BC	14–15	Bulk	Beta A.	**2,590 ± 30**	2,284 ± 93
CAS16-06PC	2–3	Bulk	Beta A.	7,850 ± 30	8,293 ± 76
CAS16-06PC	204–205	Bulk	LMC	5,330 ± 30	5,674 ± 87
CAS16-06PC	235.5–236.5	*G. sacculifer*	Beta A.	8,670 ± 30	9,324 ± 85
CAS16-06PC	244.5–245.5	*G. sacculifer*	Beta A.	9,970 ± 40	11,047 ± 107
CAS16-06PC	596–597	*N. Dutertrei*	Beta A.	34,480 ± 240	38,848 ± 304
CAS16-07PC	8–9	*G. ruber alba*	Beta A.	7,460 ± 30	7,888 ± 77
CAS16-07PC	14–15	*G. ruber alba* and *rosea*	Beta A.	10,440 ± 30	11,714 ± 120
CAS16-07PC	44–45	*G. trilobus, G. sacculifer*	Beta A.	**5,300 ± 30**	5,641 ± 86
CAS16-07PC	98–99	*G. ruber alba*	LMC	**6,990 ± 30**	7,445 ± 73
CAS16-07PC	120–121	*G. trilobus, G. sacculifer*	Beta A.	**8,660 ± 30**	9,313 ± 87
CAS16-07PC	158.5–159.5	Bulk	Beta A.	**10,330 ± 40**	11,540 ± 128
CAS16-07PC	1,093–1,094	*G. sacculifer*	Beta A.	>43,500	
CAS16-14PC	5–6	*G. ruber alba*	LMC	16,330 ± 70	19,002 ± 135
CAS16-14PC	18–19	Bulk	Beta A.	15,280 ± 40	17,885 ± 132
CAS16-14PC	485.5–486.5	*G. ruber, G. sacculifer*	Beta A.	10,400 ± 30	11,649 ± 122
CAS16-14PC	493.5–494.5	Bulk	LMC	9,630 ± 35	10,557 ± 106
CAS16-14PC	517.5–518.5	*G. ruber alba, G. trilobus, G. sacculifer*	LMC	8,345 ± 35	8,905 ± 106
CAS16-14PC	667–668	*G. ruber*	LMC	**9,515 ± 40**	10,399 ± 101
CAS16-14PC	682–683	*G. ruber rosea*	LMC	**13,300 ± 60**	15,373 ± 135
CAS16-14PC	983–984	Bulk	LMC	>44,900	
CAS16-14PC	1,035–1,036	Bulk	LMC	34,630 ± 550	38,894 ± 644
CAS16-14PC	1,573.5–1,574.5	*G. ruber alba*	LMC	47,200 ± 2,600	50,151 ± 2,560
CAS16-14PC	2,255.5–2,256.5	Bulk	LMC	Indistinguishable BS	
CAS16-31PC	275.5–276.5	*G. ruber alba*	LMC	**4,280 ± 30**	4,407 ± 99
CAS16-31PC	358.5–359.5	*G. ruber, G. trilobus, G. sacculifer*	Beta A.	**4,950 ± 30**	5,255 ± 102

Table 2
Continued

Cores	Sample intervals (cm)	Natures of sample	Lab.	Radiocarbon age (BP)	Calibrated age (BP)
CAS16-31PC	1,255.5–1,256.5	*G. ruber alba*	LMC	**6,500 ± 30**	6,953 ± 96
CAS16-32BC	1–2	*G. sacculifer*	Beta A.	**2,350 ± 30**	1,990 ± 91

Note. The ages are calibrated with OxCal software (Bronk Ramsey, 2009) using the MARINE 20 curve (Heaton et al., 2020) and the delta *R* recalculated from Paterne et al. (2018). The cal BP ages are indicated by their mean ± standard deviation. Ages indicated in bold form the input information of the age-models.

Bronk Ramsey & Lee, 2013) to construct an age-depth model of event-free sediment sections, which we built for each core by removing all instantaneous event deposits. The regularity of the sedimentation rate into the model is determined by the *k* factor, which we chose to be equal to 1 (Bronk Ramsey, 2008; Bronk Ramsey & Lee, 2013). When two cores were sampled in a basin at the same location (i.e., a piston core and an interface box-core), we merged the information obtained from both cores to build the age-depth model. On two cores (CAS16-14PC and CAS16-04PC), we also counted specific foraminifera species in 150 μm-sieved hemipelagic samples (*Globorotalia* (*G.*) *menardii* group—including *Globorotalia menardii*, *Globorotalia tumida* and *Globorotalia tumida flexuosa*—and *Pulleniatina obliquiloculata*) as broad markers of both chronostratigraphy and paleoclimate. At tropical and subtropical latitudes, the *G. menardii* group is almost absent during glacial periods and the species *G. tumida flexuosa* disappeared 81 Kyr ago, at the Marine Isotope Stage (MIS) 5/MIS 4 transition (Ericson & Wollin, 1956; Reid et al., 1996). The species *P. obliquiloculata* was temporarily absent in the Caribbean at the onset of MIS 3 (Rama-Corredor et al., 2015) and it also appears earlier and disappears later than the *G. menardii* complex during glacial/interglacial transitions (Prell & Damuth, 1978).

We performed a core-to-core correlation of the event deposits by combining multiple proxies: the seismic stratigraphy of the basins imaged by the SBP profiles; the ^{14}C dates; the physical and geochemical properties of the hemipelagic deposits (Magnetic Susceptibility, gamma density, and XRF ratios) as well as information from the sediment facies.

4. Results

4.1. Seismic Stratigraphy of the Sampling Sites

Several SBP profiles imaged the infill of the sampled basins down to about 50 m below the seafloor (Figures 2 and 3). The seismic stratigraphy of the three sampled basins of the Désirade Trough, the Falmouth and Caravelle Half Grabens, and the Désirade Basin, is strikingly similar. Three units (U1 to U3 from top to bottom) can be distinguished (Figure 2). U1 is made of strong sub-parallel reflections alternating with thick acoustic transparent layers that we named tl 1 to tl 4. Those layers uniformly drape the center of the basin floor and pinch out near the edges of the basins. The unit U2 is also an acoustically transparent layer showing the same geometry but being much thicker. The unit U3 shows the same pattern as U1 but is characterized by lower-amplitude reflections (Figure 2). In the other three basins, the Barbuda, Méduse and Karukera Basins, the seismic stratigraphy is different: the Barbuda Basin sedimentary infill is characterized by strong reflections alternating with at least three thick acoustically transparent layers (Figure 3a), whereas the Méduse and Karukera Basins contain numerous horizontal, highly reflective and thinly stratified layers (Figures 3b and 3c). We identified two lens-shaped thick transparent units, which we interpret as mass transport deposits (MTD) intercalated in the main sedimentary units in the Falmouth Half Graben (Figure 2b) and in the Méduse Basin (Figure 3b). The MTD in the Falmouth Half Graben was partly described by Seibert et al. (2020) from bathymetry and backscatter data: they identified a headscarp on the steep slopes of the accretionary wedge in the bathymetry and a fan deposit in the backscatter data (yellow dashed line in Figure 2a); in the SBP profile CAS-36, which crosses the fan deposit, we highlight a thick lenticular acoustically transparent unit which is embedded within horizontal and sub-parallel sedimentary layers of the unit U1. The base of the deposit corresponds to the base of the tl 2 transparent acoustic layer. The Falmouth Half Graben is thus likely fed both by sediments transported by the Willoughby Canyon and by deposits originating from landslides on the steepest slopes of the accretionary wedge (Figure 2a). In the Méduse Basin, the MTD is observed on the eastern edge of the basin. The basin floor is also covered by several hundred-meters large blocks visible in the bathymetry but also in the SBP profile CAS-74 as hyperbolae (Figure 3b).

By converting the SBP vertical scale from two-way travel time to depth using the mean P-wave velocity measurements obtained on the cores (1,700 m/s for core CAS16-01PC, 1,300 m/s for core CAS16-07PC, and 1,500 m/s
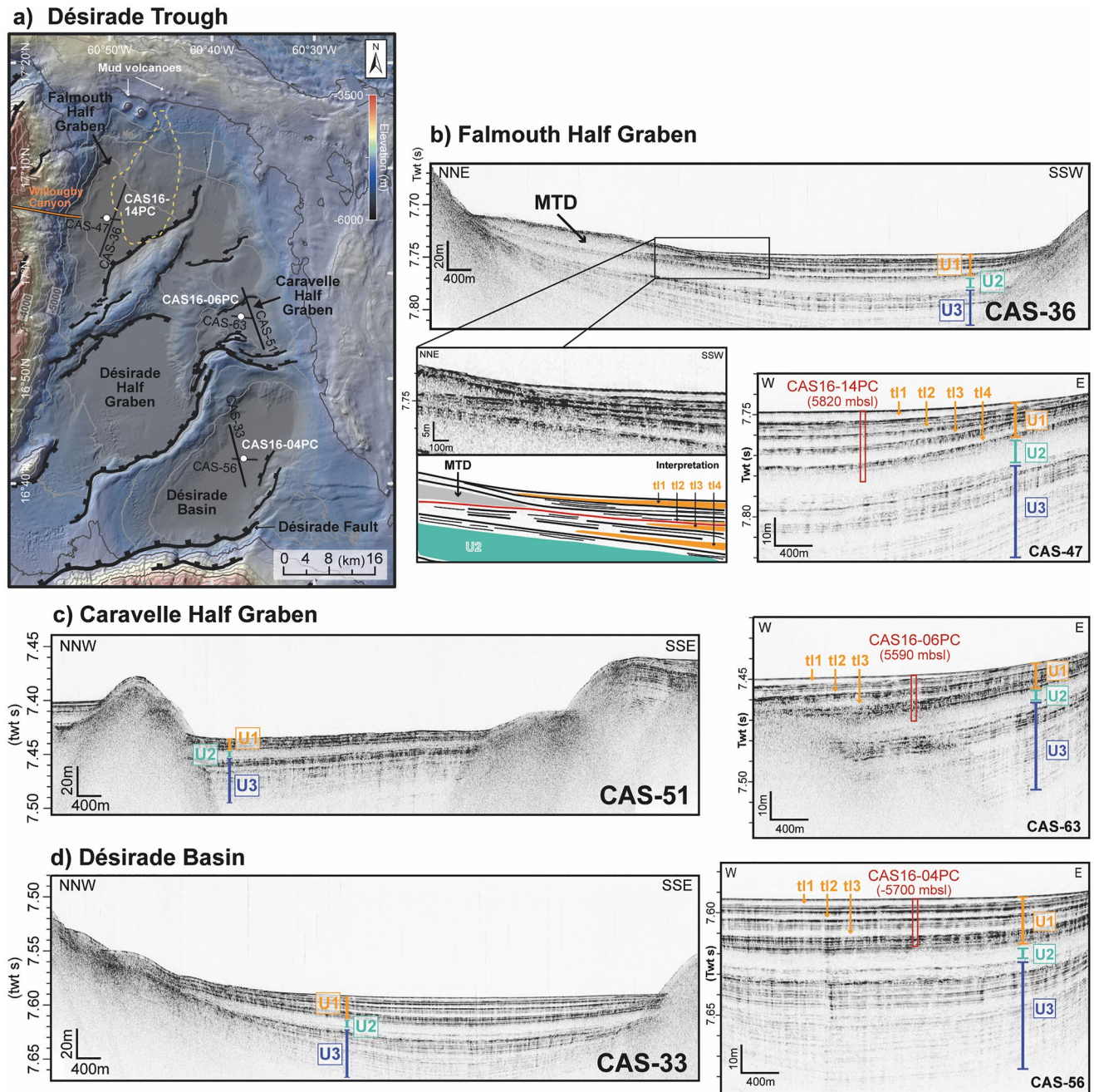
Figure 2. Map and Sub Bottom Profiles (SBP) of the Desirade trough. (a) Map of the Désirade Trough (located on Figure 1b), with the locations of cores (white dots). Black lines represent the location of the SBP. Yellow dotted line: the extension of the MTD identified by Seibert et al. (2020). (b) SBP of the Falmouth Half Graben; the southern edge of the mass transport deposit (MTD) highlighted in SBP CAS-36 is interpreted, red line highlights the MTD basal reflector. (c) SBP of the Caravelle Half Graben. (d) SBP of the Désirade Basin. TWTT: two-way travel time. We defined 3 acoustic facies: u1 (orange segment), u2 (green segment) and u3 (blue segment); the thick seismic transparent layers within the u1 are labeled tl. The SBP CAS-47, CAS-63, and CAS-56 were acquired with the research vessel drifting with propellers turned off to lower the noise. The red rectangles on them indicate the location and penetration of the core into the basins.

for the four other cores; Supplementary 2 in Supporting Information S1), we can determine which acoustic unit was sampled at each site. We sampled the whole unit U1 in all basins of the Désirade Through and reached the top of the unit U2 in the Caravelle and Falmouth Half Graben (Figure 2). In the Barbuda Basin, we cored the first two thick transparent upper units (Figure 3a). In the Méduse Basin, the core was long enough to cross the MTD (Figure 3b). In the Karukera Basin, the core was shorter and reached the base of one of the strongest acoustic reflectors (Figure 3c). We sampled only the topmost stronger reflectors.
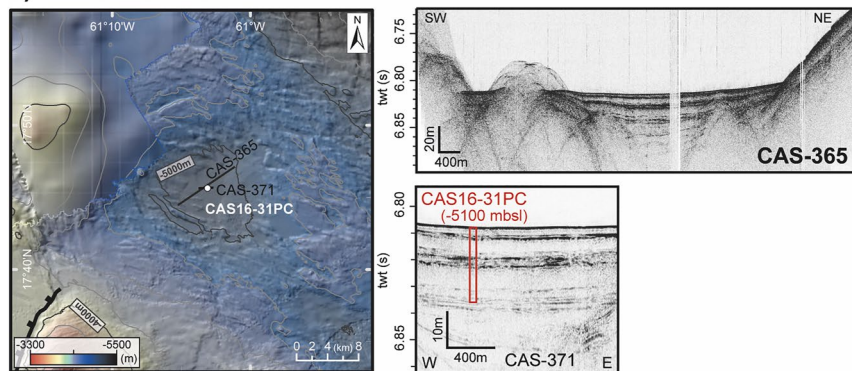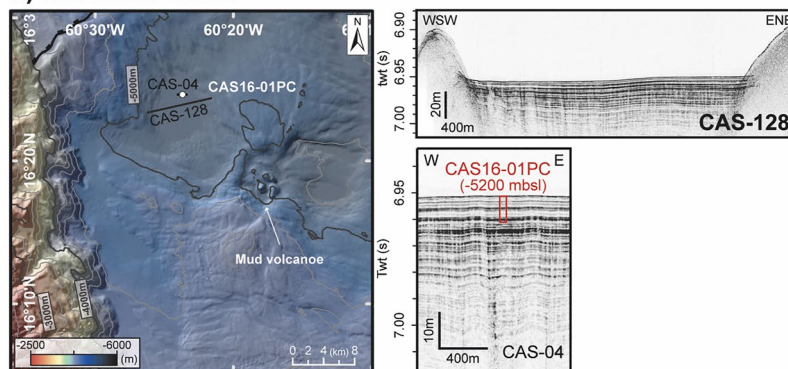
Figure 3. Maps (Located on Figure 1b) and Sub Bottom Profiles (SBP) of the Barbuda Basin (a), Méduse Basin (b) and Karukera Basin (c). The SBP CAS-371, CAS-80 and CAS-04 were acquired with the research vessel drifting with propellers turned off to lower the noise. The red rectangles on the SBP correspond to the location and penetration of the core into the basins.
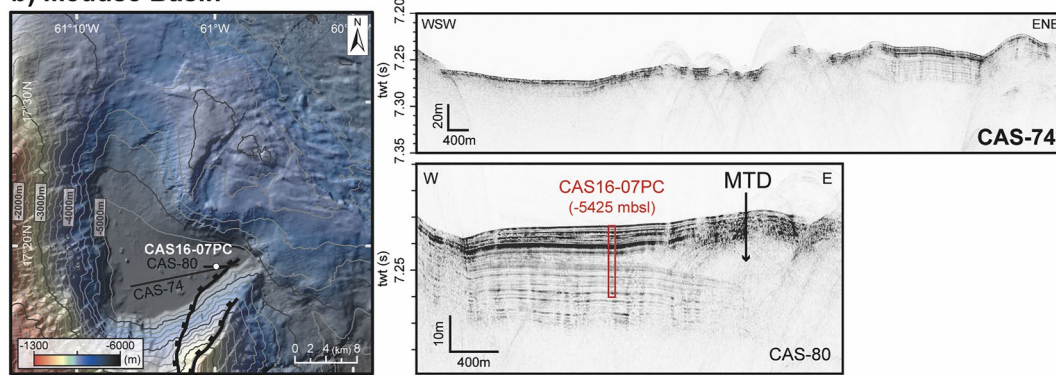
4.2. Sediment Cores

4.2.1. Lithology

Photographs, X-rays, description, and physical and chemical properties of the cores are shown in supplementary S2 in Supporting Information S1. To characterize deposits, we choose to retain three ratios, the Si/Ca and Sr/Ca ratios and the Ti/Ca log ratio, as they were the most useful for our correlation and are the most relevant to observe variations. The Ti/Ca ratio indicates the relative variations of terrigenous and marine carbonate inputs and the Sr/Ca ratio indicates the presence of high-Sr aragonite from shallow water carbonate sources, respectively (Croudace et al., 2006). We used the Si/Ca ratio because it highlights strong variations in the biogenic silicate and terrigenous content of these cores. In the here-analyzed setting, the interpretations of these parameters are

based on the three main possible initial provenances: (a) local planktonic production settling, (b) lateral input from the arc, and (c) lateral input from the accretionary wedge (Barbados Prism). Provenance 2 has to be divided into volcanic material and platform shallow carbonate. Provenance 3 may be strongly influenced by a continental South-American source (Deville et al., 2015, and references therein). Thus, provenances 2 and 3 are inferred to be recorded through Sr, Si, and Ti relative variations. Ca content may be related to provenances 1 and 2, not excluding the Barbados Prism, which also comprises calcareous hemipelagites.

The six cores are all composed of hemipelagic sediments interbedded with event deposits (Figure 4). Close-up views of the cores show the different facies encountered (Figure 5). Hemipelagic intervals can be easily recognized as they are bioturbated or faintly stratified/laminated on X-ray (Figure 5). Visual observations show that the sediment, with colors varying from greenish to brownish, consists mainly of fine sediment with more or less coarse-grained content (biogenic and detrital fractions). We distinguish two main hemipelagic facies with distinctive chemical content, color and texture. The first one (Hmp L on Figure 5) is made of fine sediment with high Ti/Ca ratio values (Figure 6). When a coarser fraction is present, it is composed of foraminifera (sometimes strongly dissolved and/or broken), quartz and ferromagnetic materials (minerals or very smoothed volcanic lithic clasts). The second hemipelagic facies (Diatom-rich Hmp L on Figure 5) consists of dark-colored sediment and a low radio-density (Figure 5) with a high Si/Ca ratio (Figure 6). It has a mushy texture and contains many diatom frustules (mostly *Ethmodicus rex*).

Deposits with a sharp basal limit, mostly normal grading from sand to clay grain size particles, and with planar or oblique laminations are parts of the classical turbidite sequence as defined by Bouma (1962). They are several centimeters to decimeters thick and can show convolutes, laminae and micro-faults (Figure 5). Accurately identifying the top of the turbidites is difficult because of the gradual transition from turbidite tails to the overlying hemipelagic deposits. Moreover, the sediments at this transition are often mixed by bioturbation, making the distinction even more challenging. Although several event deposits show a nearly complete Bouma turbidite sequence, most of them are characterized by a sharp transition from the coarse to fine-grained parts (Figure 5), the lack of a coarse base, or by several coarse-grained pulses (Figure 5). When these pulses are not separated by clay layers, we considered such intervals as a single amalgamated turbidite, as documented in similar contexts (Migeon et al., 2017; Van Daele et al., 2017; Wils et al., 2021). As the distinction between amalgamated-turbidite (i.e., multi-pulsed flows) and series of stacked single turbidites is not straightforward (Van Daele et al., 2017), additional grain size measurements are however necessary to support this interpretation. In all cores, the lowest values of Log(Ti/Ca) are observed in the coarse levels of sedimentary events. The turbidites are labeled per core from top to bottom (Figure 4).

In four cores CAS16-04PC, CAS16-06PC, CAS16-14PC, and CAS16-31PC taken in the Désirade Basin, Caravelle Half Graben, Falmouth Half Graben and Barbuda Basin, respectively (Figure 1b), several meters-thick layers of unbioturbated mud are characterized by homogeneous geochemical ratios and magnetic susceptibility values (Figures 4 and 6). They strikingly correspond to the acoustically transparent units imaged in the SBP and described earlier (Figures 2 and 4 and Supplementary S2 in Supporting Information S1). In core CAS16-14PC, each homogeneous unit (Hm 1 to 4 on Figure 4) readily correlates with seismic units tl 1 to tl 4 (Figure 2a, profile CAS-47 and Figure 4, stationary SBP). The thicker homogeneous unit Hm 5 corresponds to the top of the thicker transparent unit 2 (Figure 4). These homogenous sediment layers overlay thick turbidites (Figure 4), with in between an interval characterized by convolute-like structures. Those homogenous deposits were observed elsewhere overlying or not turbidites (e.g., in the Mediterranean sea, Kastens & Cita, 1981; in the Marmara sea, Beck et al., 2007; or in Japan, Kioka et al., 2019; McHugh et al., 2020) and were linked to great earthquakes or tsunamis (i.e., the March 2011 Tohoku earthquake in Japan, Kioka et al., 2019; McHugh et al., 2020). When the homogenite overlays a turbidite, the entire sequence is named HmTu (Homogenite + Turbidite) following the nomenclature of Beck et al. (2007), with the homogenite corresponding to the thick mud deposit. Based on those previous studies, we named our deposits as HmTu and considered the complex turbidite plus homogenite as a unique event deposit. We discuss their possible origins later in the discussion part.

Based on the selected XRF ratio, log ratio, scatter plots and physical parameters, we classified the event deposits into five families: calci-rich, aragonite-rich, calci-aragonite-rich, terrigenous-rich, and diatom-rich event deposits (Figure 6, Supplementary S3 in Supporting Information S1 for details). We notice that the cores CAS16-04PC and CAS16-06PC contain more aragonite-rich turbidites (Figure 6, Supplementary S3 in Supporting Information S1). The coarse fraction (>63 μm) of the event deposits in cores CAS16-04PC and CAS16-14PC contains calcareous biogenic particles (well-preserved or fragmented planktonic or benthic foraminifera, pteropods, and
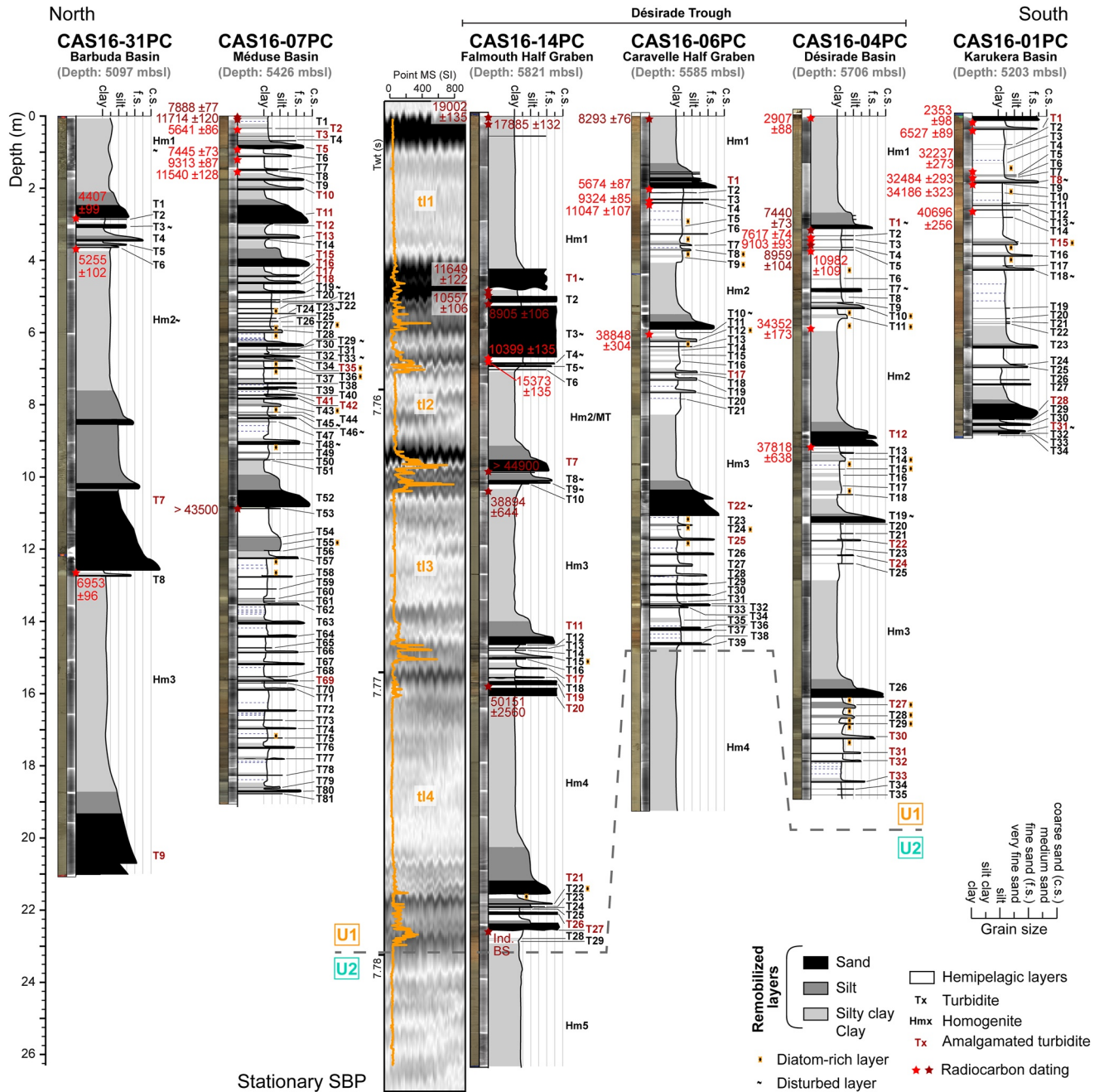
Figure 4. Sedimentological logs of the six cores, located on Figure 1b, including the results of the radiocarbon dating (cal BP, mean ± standard deviation). The grain size was determined visually. The red stars show the radiocarbon ages used within the age-model, and the dark red stars have not been integrated to the age-model either because they show inverse ages or because they are out of the limit of radiocarbon dating. The labeling of the turbidite deposits is numbered independently on each core, Hm: homogeneous mud layers. On the left of the CAS16-14PC core is shown its stationary SBP acquired during the coring operation, with magnetic susceptibility (MS) curve. The gray-dotted line highlights the limit between the seismic U1 and U2 over the Désirade Trough basins. The purple-dotted lines correspond to undetermined deposits (potential turbidites, though not integrated into the turbidite label).

siliceous biogenic particles—mainly sponge and/or holothurids spicules and diatoms) and terrigenous particles (lithic fragments, aggregated or not with calcareous cement, isolated minerals such as quartz, plagioclase feldspar, pyroxene, amphibole, opaques or glass shards). Several rare, but significant, elements are observed in some event deposits, such as ostracods or bryozoans (Supplementary S3 in Supporting Information S1). From the sediment content, it is possible to make assumptions on the source of the event deposits (Volcanic Arc—VA, Arc calcareous platforms—ACP, fore-arc basin slopes—FABS, see Tables S3-1 and S3-2 in Supporting Information S1).
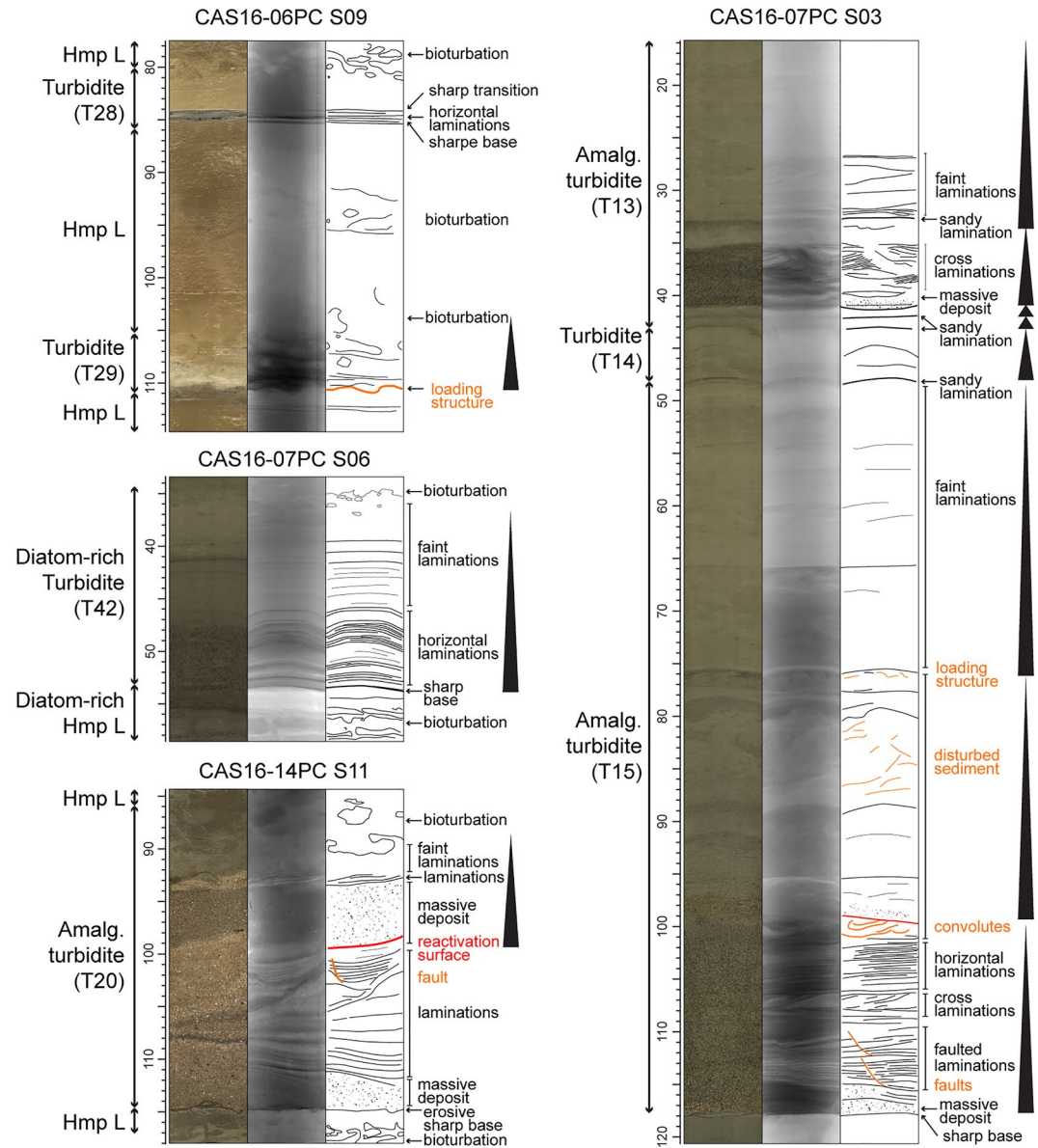
Figure 5. Details of the sedimentological facies. Each facies is illustrated by the photographs (on the left), the X-ray images (on the right) and the sketch of the main features of the core. The vertical scale is in centimeters and corresponds to the depth in the section (S). Black triangle: normal graded of the grain size; Hmp L: Hemipelagic Layer; Amalg.: Amalgamated, Tx: labelling of the turbidite according to Figure 3.

However, we need to remain cautious as we analyzed only the >63 µm fraction and the composition can be significantly influenced by mechanical sorting during the transport and/or settling, as several reworkings may have occurred. Fresh pyroxene (augite) and amphiboles (hornblende) grains, as well as plagioclase feldspars, and rare glass shards are likely sediments remobilized from submarine slopes close to the volcanic arc, or from remote primary or secondary (already remobilized) tephra deposits. Event deposits made of benthic foraminifera and bioclasts may be the result of the remobilization of sediments coming from shallow reef environments (ACP). The presence of planktonic foraminifera and pteropods suggests that the sediments may originate from deeper environments such as the forearc basin's slopes (FABS). The pteropods could be the sources of aragonite in calcitic/aragonitic rich event deposits in the core CAS16-14PC. Event deposits in core CAS16-04PC are also notably enriched in fragments of Homotrematidea (*Miniacina sp*.) and Bryozoa, indicating material from shallow reef down to upper slope environments. The amalgamated turbidites are made of sediment pulses of various contents, implying different sources. Fragmented *E. rex* diatoms were observed in hemipelagic and turbidite
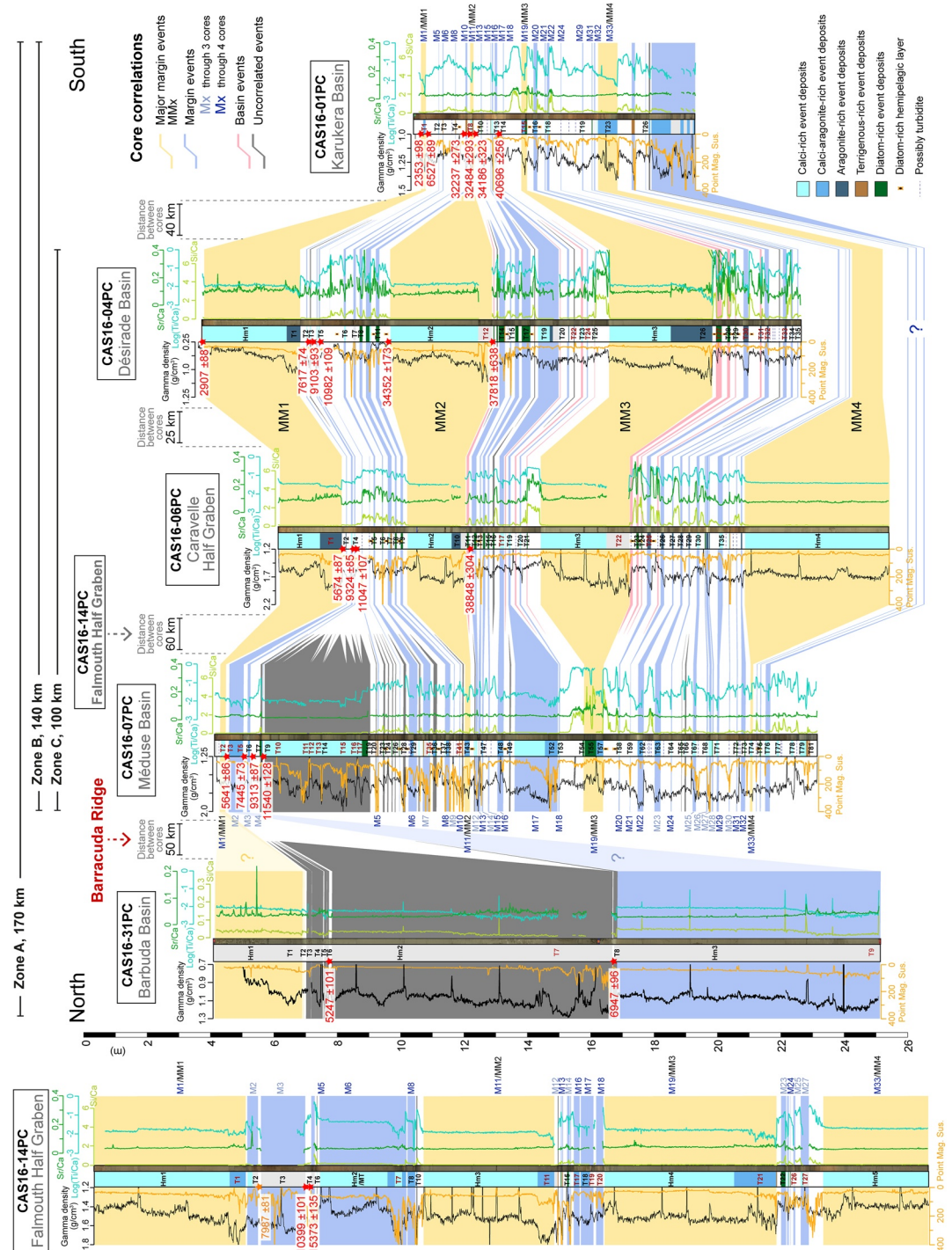
Figure 6. Turbidite correlation between the cores, showing the photo of the cores, the turbidite composition, the geophysical and geochemical data (Gamma density, Punctual magnetic susceptibility—*10⁵ SI, Si/Ca, Log (Ti/Ca) and Sr/Ca). The red stars are the radiocarbon dates used within the age models; the orange star on the CAS16-14PC core corresponds to a radiocarbon date obtained on a sample of the CAS16-03PC core, with the same location of the CAS16-14PC core (Figure 1b) and the same stratigraphy (Figure S1-1 in Supporting Information S1). To improve the visualization, the top of the cores is not aligned, but all the cores have the same scale. Yellow correlations: Major Margin events; blue correlations: Margin events; red correlation: Basin events; and gray intervals are for the uncorrelated events.

deposits in all cores except CAS16-31PC (Figure 4). We further used them as biological markers to help in the correlation of the event deposits between cores.

4.2.2. Radiocarbon Dating

To establish the chronology of the event deposits, we obtained 43 radiocarbon ages on planktonic foraminifera collected in the hemipelagic intervals in all cores, including the box-cores (see details on the samples and dates in Table 2). The samples were mainly collected below or just above the event deposits, when the top of the event deposit was clearly identified, as well as in the hemipelagic intervals. It was difficult to find datable material and obtain several reliable ages for the same hemipelagic intervals as they are thin and the water depth in the basins where the cores were collected is close to the Carbonate Compensation Depth (CCD). Published overviews for the Atlantic mention a CCD at a 4,500–4,800 m depth (Dutkiewicz & Müller, 2022), but calcareous hemipelagic sediment (17.8% $CaCO_3$) has been cored at a 4,980 m depth along of the Barbados Prism's deformation front (Wang et al., 1990). These deep occurrences may be explained either by a regionally deeper CCD (influenced by the active geodynamic setting) or by local reworking of calcareous hemipelagites previously deposited in shallower areas.

All the ages are plotted with the core descriptions (Figure 4). Several ages are inverted or inconsistent, likely due to bioturbation, surficial remobilizations, erosion, or coring perturbations. As examples, the samples collected at the top of piston cores CAS16-14PC, CAS16-06PC, and CAS16-07PC are much older than others, whereas those collected in the neighboring box-cores are much younger, suggesting bias due to coring. We discarded those samples and selected 27 ages to build event-free chronostratigraphic models (Figure 7, Table 2). From those models, we estimated mean apparent sedimentation rates over the last 40 Kyr (Figure 7). The compaction of the sediment as revealed by the trend in whole core P-wave velocity appears to be limited. The sedimentation rates may be over-estimated by 25% due to stretching of the uppermost sediment pile, as estimated from CINEMA. Basal erosion by turbidity currents could be the main source of bias in the estimation of the sedimentation rates. This is well illustrated by the age-depth models elaborated for core CAS16-01PC. In the uppermost part of the core, the apparent sedimentation rate, which is calculated from radiocarbon dates of samples collected above and just below the turbidite T1, is found to vary from 0.7 to 4.5 cm/Kyr. The base of the event deposit T1 forms a sharp contact with the hemipelagic sediments underneath, suggesting an erosive contact. We noticed that the hemipelagic layers are thinner than elsewhere in the CAS16-14PC core, possibly due to stronger erosion by turbidity currents at the mouth of the Willoughby canyon where the core is located (Figure 1b). Erosion is likely to occur in proximal canyon sites and is greatly reduced in distal sites. Apparent sedimentation rates vary within a core and between cores and range between ~1 and 15 cm/Kyr, in agreement with previous estimates by Reid et al. (1996) and Bieber et al. (2021) in the fore-arc domain. The age-depth models of the hemipelagic sediments in the Désirade and Barbuda Basins are well constrained from radiocarbon dates in both piston and box cores with an age zero or slightly older for the sediment/water interface (Figure 7). This is not the case for other sites for which the top of the piston core was not doubled by a parallel box-core. The sediment/water interface may be as old as 5 Kyr, meaning that either the age model is less well constrained or that we lost a few centimeters of the sediment/water interface. Comparisons with piston and box-cores indicate that we lost the 9.5 and 4 upper centimeters of sediment, respectively, in the Désirade Basin in core CAS16-04PC and in the Barbuda Basin in core CAS16-31PC (Supplementary S1 in Supporting Information S1).

4.2.3. Other Chronological Constrains

The foraminifera species assemblages indicate that we cored sediments of the MIS 5 in the Falmouth Half Graben (CAS16-14PC) but not in the Désirade Basin (CAS16-04PC) (Figure 8; tables with the data in Supplementary S4 in Supporting Information S1). This MIS5/MIS4 transition (estimated at 81 Kyr in the Lesser Antilles from Reid et al. (1996)) is marked by the disappearance of *G. tumida flexuosa* that is located somewhere between 97 and 112 cm (in between the two samples, Figure 8) in the event deposits-free core CAS16-14PC. In this core, the *P. obliquiloculata*, whose extinction occurred about 34–35 Kyr ago in the equatorial Atlantic (Prell & Damuth, 1978; Wilson, 2008), disappear above ~70 cm. The *G. menardii* group, which is a marker of MIS1 glacial/interglacial transition, appears above 30 cm. Overall, this suggests that the sediments of this depth interval (30–70 cm) are 34–35 to 14 Kyr old.

4.2.4. Event Deposits

Numerous event deposits were found in all cores. We numbered them independently between cores as Tx for turbidites and Hmx for homogenites (Figure 4, Supplementary S2 in Supporting Information S1). We identified 34, 35, 39, 81, 29, and 9 turbidites in cores CAS16-01PC, -04PC, -06PC, -07PC, -14PC and -31PC, respectively, and 3,4,5 and 3 homogenites in cores CAS16-04PC, -06PC, -14PC and -31PC, respectively (Figure 4). No homogenites were
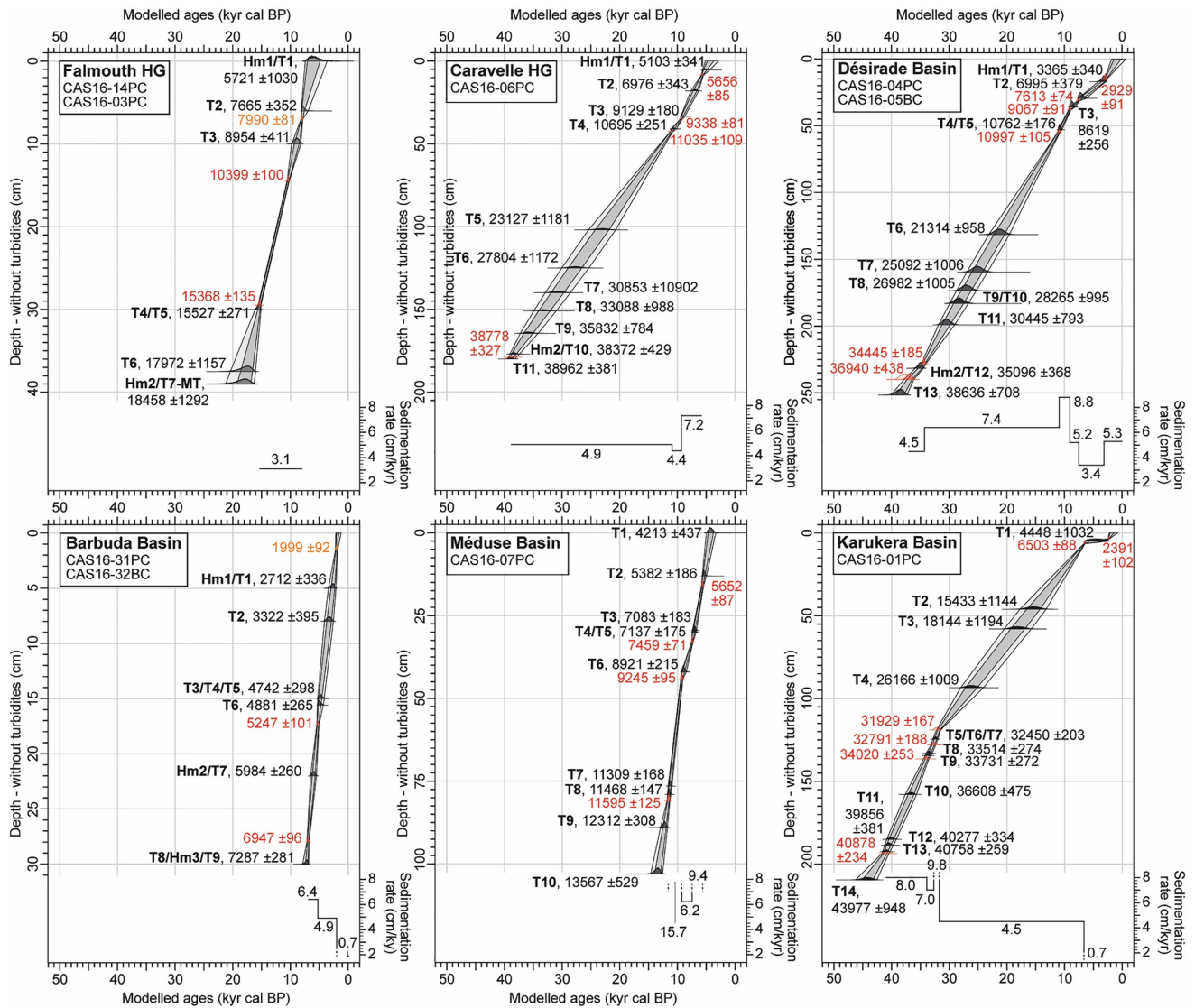
Figure 7. Age model established for event deposits free core (hemipelagic section depleted from event deposits) with Oxcal 4.4 program (Bronk Ramsey, 2009) by using the Marine 20 calibration curve (Heaton et al., 2020), the recalculated reservoir age Δ*R* value recalculated from Paterne et al. (2018) and a *k* parameter of 1. Modeled radiocarbon ages are indicated in red and the turbidite age distributions are in black, both with the mean and standard deviation, Dark gray interpolated interval: 1-sigma probability (68.3%), light gray interpolated interval: 2-sigma (95.4%). The apparent sedimentation rates are estimated from radiocarbon ages. The radiocarbon ages indicated in orange in the Falmouth Half Graben and in the Barbuda Basin age models were sampled in the core CAS16-03PC and the box-core CAS16-31PC, respectively. The indication from the comparison between the cores CAS16-04PC and -05BC that 9.5 cm of hemipelagic sediment were lost during the piston coring has been integrated into the age model.

found in the cores CAS16-01PC and -07PC. The turbidite thickness range between ∼0.5 and ∼100 cm. The Hm/Tu are much thicker (between ∼200 and ∼900 cm). In all cores, we identified amalgamated turbidites (indicated with numbers in red on Figure 4). We identified an impressive stack of ten calci-rich turbidites (including amalgamated turbidites) in core CAS16-07PC (T9-T19, Figure 4). No event deposits could be distinguished with the data currently available in the box-cores. From the age-depth model, it is possible to estimate the ages of the event deposits younger than 50 Kyr (Figure 7). Almost the same numbers of event deposits were emplaced during the last 40 Kyr in the neighboring Désirade Basin, Caravelle Half Graben and Karukera Basin (13, 11, and 13 in cores CAS16-04PC, -06PC, -01PC, including two homogenites in cores CAS16-04PC and -06PC respectively). Six event deposits (including 2 homogenites) were emplaced in the Falmouth Half Graben (CAS 16-14PC) and 10 event deposits in the Méduse basin (CAS16-07PC) over the last 20 and 14 Kyr, respectively. It is noteworthy that turbidites are missing in cores CAS16-04PC and -06PC between 20 and 10 Kyr (Figure 7). The core CAS16-31PC shows a contrasting sedimentary record with nine event deposits only, among which three HmTu younger than 7 Kyr (Figures 4 and 7).
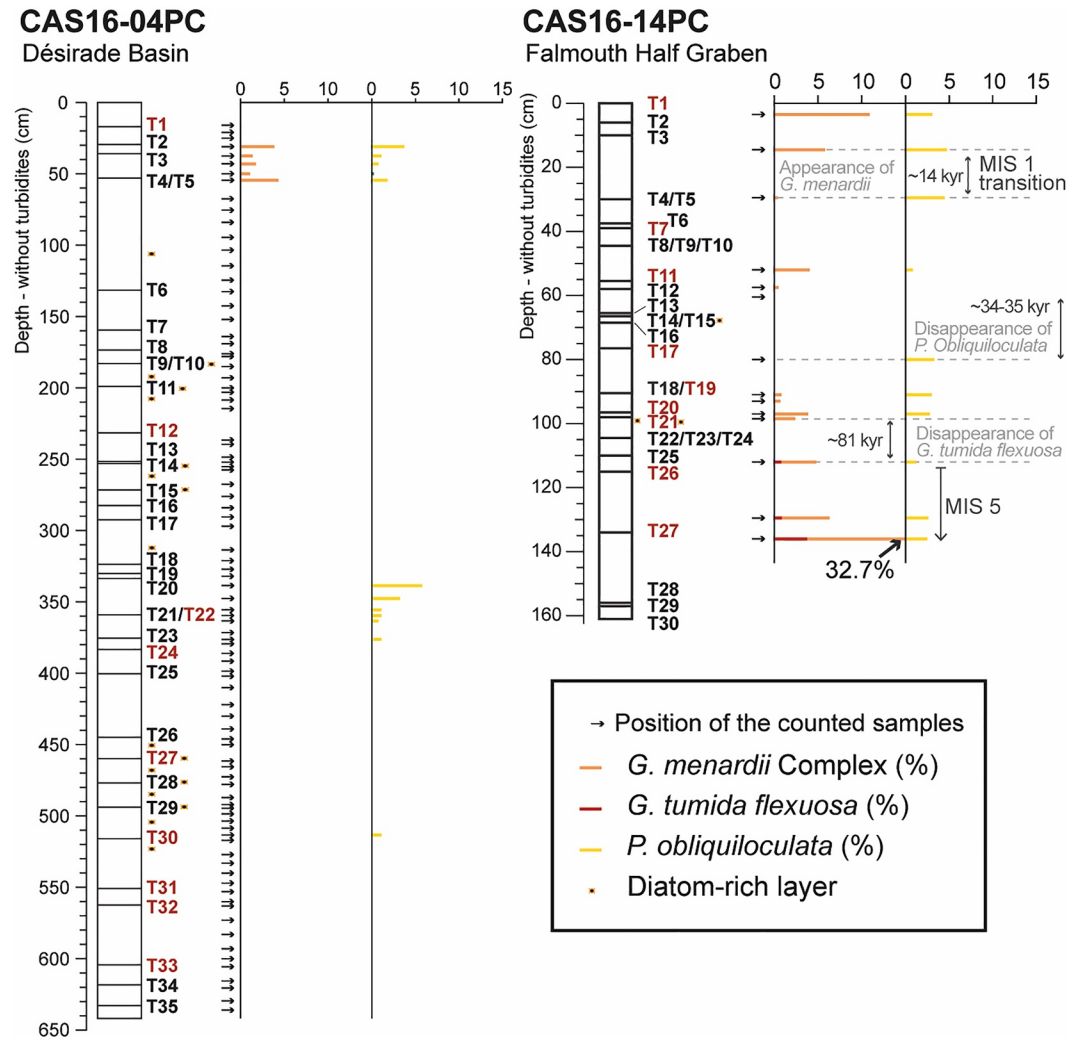
Figure 8. Biostratigraphic limits from the abundance of *G. menardii Complex*, *P. obliquiloculata* and *G. tumida flexuosa* (%) along cores CAS16-04PC and CAS16-14PC MIS: Marine Isotope Stages.

4.3. Interbasin Correlations

We classified the events responsible for the event deposits (HmTu, homogenite, turbidites amalgamated or not, MTD) in four families and discuss their origins later in the discussion section: (a) "Margin events" (M events) that triggered synchronous turbidites recorded in at least three cores sampled in three different basins; (b) "Major Margin events" (MM events), that triggered synchronous HmTu deposits in three different basins; (c) "Basin events" (B event) that triggered turbidites in two adjacent basins; and (d) "Local events" are events that triggered a turbidite in one basin only. For clarity and continuity in the numbering of the M events, we attributed an M event-number to each MM event (e.g., MM1 event is also the M1 event, MM2 event is the M11 event, Figure 6). In distant cores, the MM event deposit can be either an HmTu deposit or a turbidite.

4.3.1. Physical and Chemical Properties Correlations

We used the Gamma density, the magnetic susceptibility and XRF measurements (Si/Ca, Log(Ti/Ca) and Sr/Ca) as "wiggle" traces that we stretched or squeezed to correlate the sedimentary units from one core to another (Supplementary S5 in Supporting Information S1, and correlation on Figure 6). In this way, we clearly identified specific sediment signatures as tie points for correlation and those are used together with constraints from radiocarbon ages. As an example, in core CAS16-01PC, -04PC, -06PC, -07PC we recognized an about 40 cm-thick hemipelagic interval clearly depleted in Ca (with high Si/Ca, Ti/Ca, and Sr/Ca ratio) that can be used confidently to correlate the MM3/M19 event deposits from a core to another one (Interval A in Supplementary S5 in

Supporting Information S1). In between homogenites, the hemipelagic intervals have physical and chemical signatures that can be used to correlate the event deposits between distant sites. This is particularly clear for the correlations between CAS16-04PC and -06PC. For instance, between the MM1 and MM2 event deposits, the chemical "bell-shaped" signature is strikingly similar between the two cores (Interval B in Supplementary S5 in Supporting Information S1). This observation can be confidently used to correlate the MM1 and the MM2 events-deposits between distant cores. Having correlated the MM event deposits between cores, it was further possible to correlate the turbidites from one core to another one (Supplementary S5 in Supporting Information S1). To reinforce our correlations, we used hemipelagic layers enriched in *E. rex* as specific markers. The MM1/M1 event promoted at least three HmTu deposits (Hm1T1 in core CAS16-04PC, -06PC, -14PC in the Désirade Trough sub-basins), one turbidite (T2 in CAS16-07PC in the Méduse basin) and one amalgamated turbidite (T1 in the CAS16-01PC in the Karukera Basin) (Figure 6). The MM2-M11 event promoted at least three HmTu deposits (Hm3T11 in core CAS16-14PC in the Falmouth Half Graben, Hm2T10 in core CAS16-06PC in the Caravelle Half Graben, Hm2T12 in core CAS16-04PC in the Désirade Basin) and one amalgamated turbidite (T8 in CAS16-01PC) and one turbidite (T43 in core CAS16-07PC). The MM3/M19 event promoted at least three HmTu deposits (Hm4T21 in core CAS16-14PC, Hm3T22 in core CAS16-06PC and Hm3T26 in core CAS16-04PC), a stack of 3 turbidites (T55-T57 in core CAS16-07PC) and an amalgamated turbidite (T15 in core CAS16-01 PC).

4.3.2. Seismic Stratigraphic Correlation of HmTu Deposits

The Désirade Trough sub-basins show comparable seismic stratigraphy in the SBP, but the number of acoustically transparent units differs in the seismic unit U1 (Figure 2). The three cores sampled in those basins (CAS16-04PC in Désirade Basin, CAS16-06PC in Caravelle Half Graben and CAS16-14PC in Falmouth Half Graben) crossed or almost reached the base of this unit (Figure 2; dashed gray line on Figure 4). While cores CAS16-06PC and CAS16-04PC crossed three acoustically transparent layers in unit U1 (tl 1 to tl 3 in the SBP CAS-63 and -56, Figures 2c and 2d), CAS16-14PC crossed four (tl 1 to tl 4 in the SBP CAS-47, Figure 2b) in the Falmouth Half Graben. Our interpretation of SBP profile CAS-36 in the latter basin shows that the basal reflector of the MTD originating from the accretionary wedge (Seibert et al., 2020) is that of tl 2 (Figure 2b), which itself correlates with the base of the Hm2Tu7 deposit in core CAS16-14PC (Figure 4). The homogenite Hm2 of the Hm2Tu7 deposit is enriched in Ti and depleted in Ca compared to the other homogenites, supporting a different source (Figure 5; Figure S3-3 in Supporting Information S1). The Hm2Tu7 likely results from the lateral evolution of the local MTD due to failure on the slope of the accretionary wedge, the trace of the MTD (failure scar and deposit, Figure 2a) having been identified by Seibert et al. (2020). It is a more local event that is not correlated with other HmTu deposits. Mulder et al. (2009) proposed that such local HmTu deposits are promoted by local mass flows involving a huge amount of failed sediment (several cubic kilometers) able to move a large volume of water and initiate the oscillation at a very long wavelength of the entire water column (seiche effect). We crudely estimated a volume of ∼1 km^3 for this MTD from the shape and depth of the landslide scarp. This may have been sufficient to promote a seiche effect in the restricted deep Falmouth Half Graben. To distinguish this local deposit from other HmTu, we re-qualified it as a megaturbidite (MT in Figure 4).

The other homogenites labeled Hm1, 2, and 3, in cores CAS16-04PC and -06PC, correspond to the transparent acoustic layers tl 1, tl 2, tl 3 in SBP CAS-63 and CAS-56 (Figure 2). Those labeled Hm 1, 3 and 4 in core CAS16-14PC correspond to the transparent acoustic layer tl 1, tl 3, and tl 4 in SBP CAS-47 (Supplementary S6 in Supporting Information S1). Only the topmost part of the acoustically transparent seismic unit U2 (Figure 2) was sampled in core CAS16-06PC and -14PC (Hm 4 and Hm 5, respectively). These deposits can be correlated seismically over the three basins of the Désirade Trough and are regional event deposits, corroborating our physical and chemical properties correlations. We thus confirm that four Major Margin events (MM1 to MM4) promoted four HmTu deposits correlated regionally (Figure 6).

4.3.3. Margin-, Basin-Events and Local Events

In between the MM1 and MM2-event deposits, we identified nine M events (M2 to M10). The core CAS16-07PC contains 12 additional turbidites including the thick sequence of 10 stacked turbidites (T9 to T19; Figure 6). One turbidite remains uncorrelated in core CAS16-04PC (T3; Figure 6). Between the MM2 and MM4 event deposits, we identified deposits related to at least 20 M events (M12 to M18 and M20 to M32), 8 B events (with related event deposits identified both in the Désirade Basin and the Caravelle Half Graben) and several local events that promoted 4, 1, and 4 isolated turbidides in the Méduse Basin, Caravelle Half Graben, and Désirade Basin, respectively (Figure 6). Three of those basin-event turbidites contain material from shallow-environments and five contain a large amount of *E. rex* diatoms (Figure 6). Only cores CAS16-01PC and -07PC were long enough

to sample event deposits older than the MM4 event deposit. Three of them can be correlated with the two cores (Figure 6). The cores being separated by 120 km, those event deposits were likely triggered by an M or maybe an MM event. However, additional cores would be required to firmly conclude.

4.3.4. Chronology of the Events-Deposits From Composite Age-Depth Models

There are large uncertainties on the ages estimated from age-depth models of various cores for the MM1 event deposits. The ages range between $3,365 \pm 340$ years cal BP in Désirade Basin (cores CAS16-04PC and -05BC) and $5,721 \pm 1,030$ years cal BP in the Falmouth Half Graben (cores CAS16-14PC, -03PC) (Figure 7). Given the low sedimentation rates, very small disturbances due to basal erosion, coring, or bioturbation may be sufficient to induce significant errors in the estimates of sedimentation rates of hemipelagic intervals. The most reliable age is that obtained from the age-depth models including the information from both the piston core and the box-core in the Désirade Basin (cores CAS16-04PC, -05BC). Age-depth models for cores CAS16-06PC, -07PC, -14PC indicate that for those cores we lost the sediment/water interface, and no sample was collected above the event deposit to estimate the sedimentation rate. The age obtained for the MM1 event in the core CAS16-01PC indicates basal erosion. In this core, the $2,353 \pm 98$ years cal BP radiocarbon age was determined from a sample located 18–19 cm below the top of the core (Table 2) and 3.5 cm below a 15 cm thick layer of sand injected during the coring. Therefore, by considering that we sampled the water/sediment interface, the $2,353 \pm 98$ years cal BP radiocarbon age was obtained from a sample collected at 3.5 cm depth, implying a sedimentation rate of 1.5 cm/Kyr between 0 and 3.5 cm in the Karukera Basin. The MM1 deposit (T1) in core CAS16-01PC is located between 5 and 24 cm. By using the sedimentation rates obtained for the upper part of the core, we estimate an age of 3.3 Kyr for this event deposit in this core. This age is consistent with the MM1 deposit age obtained in the core CAS16-04PC (Figure 7). It is noteworthy that the MM1 event is much older than the historical seismic or other extreme events.

The core CAS16-31PC shows a contrasting sedimentary record. We cannot firmly correlate either with seismic stratigraphy or physical and chemical parameters, the Hm1Tu1 deposit found northward, in the Barbuda Basin (core CAS16-31PC), with others in the Désirade Trough sub-basins. Its age ($2,712 \pm 336$ years cal BP) is however coeval with others within the uncertainties (Figure 7). Given the rarity of such thick deposits, it is very likely that it was also triggered by the MM1-event or another contemporaneous major event. The Hm3T9 deposit may have been promoted by the M2 event (Figure 6). In between, the turbidites T3 to T8 could not be correlated with other event deposits in neighboring cores.

Based on our correlations, it is possible to improve the chronology of our event deposits by elaborating a composite age-depth model including all the chronological constrains available (radiocarbon and biostratigraphic benchmarks) for cores CAS16-01PC, -04PC, -06PC, and -14PC. In the Core CAS16-14PC, we placed the MIS4/MIS5 boundary dated at 81 Kyrs in the middle of the 97–112 cm depth interval in which the *G tumida flexuosa* disappeared (Figure 8) and used an arbitrary uncertainty of ± 5 Kyr at this age. Given the sedimentation rate determined from radiocarbon dating in the upper part of the core (3 cm/Kyr), this error is very conservative as we can estimate that the sediment of this depth interval (15 cm) would have been deposited in about 5 Kyr. With our composite age-depth model for the core CAS16-14PC, we estimated an age of ∼70 Kyr for the MM3 and 120 Kyr for the MM4 event deposits. We included this age for the MM3 into the other age-depth models for cores CAS16-01PC, -04PC, and -06PC (see Supplementary 7 in Supporting Information S1).

Age ranges of all MM and M events, but the M1/MM1, M3, M11/MM2 (in bold in Table 3) are the intersection between all age intervals estimated from age-depth models of each core (Table 3, Figure 9, orange dots with errors indicated as thick pink bars). The age of the M1/MM1 event is well constrained (3.3 Kyr) by radiocarbon dating above the deposits in cores CAS16-01PC, and -04PC. The age of the M3 event is well constrained by the age of the M3 event deposit in CAS16-06PC. The age of the M11/MM2 is the intersection between age intervals from age-depth models of cores CAS16-04PC and -06PC only. We determined that the MM events have occurred around 3.3, 35, 70, and 120 Kyr (Figure 9). In between the MM1 and MM2, MM2 and MM3, MM3 and MM4 events, 9 (M2 to M10), 7 (M12 to M18) and 13 (M20 to M32) M events were identified respectively. From Table 3 and Figure 9, we can infer that the inter-event intervals of the M events range between 1.8 and 12 Kyr.

4.3.5. Regional Extension of the Event Deposits

Figure 10 synthetizes our results. From our correlations, we identified 33 large M and MM events that generated synchronous sediment remobilizations. The MM1 event was likely recorded in all the cores that we sampled over an area of ∼170 km (Zone A). Nineteen M events, including 3 MM events, triggered synchronous event deposits

Table 3
Modeled Ages of Margin Event (See Main Text for Detail)

| | Margin events age (yr BP) | | | | Event deposits age (yr BP) | | | | | | | | |
| | | | | | Karukera basin (CAS16-01PC) | | | Desirade basin (CAS16-04PC) | | | Caravelle half Graben (CAS16-06PC) | | |
	Age max	Age min	Mean	Error		Age max	Age min		Age max	Age min		Age max	Age min
M1/MM1			3,365	340	T1	6,296	2,555	T1	4,084	2,830	T1	*5,645*	*4,306*
M2	7,636	6,306	6,971	665				T2	**7,636**	6,227	T2	7,659	**6,304**
M3	9,432	8,752	9,092	340				T4	*11,093*	*10,408*	T3	**9,430**	**8,750**
M4	11,094	10,418	10,756	338				T5	**11,094**	**10,418**	T4	11,123	10,173
M5	17,689	13,205	15,447	2,242	T2	**17,689**	**13,205**				–		
M6	20,480	19,587	20,034	447	T3	**20,480**	15,762	T6	23,088	19,429	T5	23,699	**19,587**
M7	26,860	23,732	25,296	1,564				T7	**26,860**	23,138	T6	27,715	**23,732**
M8	28,055	26,618	27,337	719	T4	**28,055**	24,075	T8	28,664	25,055	T7	30,209	**26,618**
M9	29,935	28,770	29,353	583				T9-T10	**29,935**	26,339	T8	31,925	**28,770**
M10	31,819	31,638	31,729	91	T5-T6-T7	32,872	31,978	T11	**31,819**	28,884	T9	33,867	**31,638**
M11/MM2	35,895	34,424	35,160	736	T8-T9	*34,216*	*33,295*	T12	**35,895**	**34,424**	T10	38,322	35,194
M12	40,611	38,808	39,710	902				T14	**40,611**	37,633	T12	41,756	**38,808**
M13	42,303	40,168	41,236	1,068	T10	**42,303**	37,362	T15	44,219	39,907	T13	44,013	**40,168**
M14	45,984	41,422	43,703	2,281				T16	46,288	41,306	T14	**45,984**	**41,422**
M15	47,185	42,948	45,067	2,119	T11	50,504	**42,948**	T17	48,152	42,638	T15	**47,185**	42,230
M16	51,707	47,605	49,656	2,051	T12	**51,707**	43,717	T19	55,012	**47,605**	T17	52,149	45,717
M17	52,807	51,629	52,218	589	T13	**52,807**	44,528	T21	60,184	**51,629**	T19	56,290	48,772
M18	57,989	54,877	56,433	1,556	T14	**57,989**	48,383	T24	64,731	**54,877**	T20	62,002	53,158
M19/MM3	74,555	63,339	68,947	5,608	T15	**74,555**	61,130	T26	75,810	**63,339**	T22	74,980	63,285
M20	80,978	72,804	76,891	4,087	T16	**80,978**	65,268	T30	88,757	**72,804**	T25	85,837	71,111
M21	88,706	79,121	83,914	4,793	T17	**88,706**	70,821	T32	97,200	**79,121**	T26	93,158	76,494
M22	90,761	84,678	87,720	3,042	T18	**90,761**	72,611	T33	104,665	**84,678**	T27	97,628	79,833
M23	103,013	86,622	94,818	8,196				T34	107,098	**86,622**	T28	**103,013**	83,510
M24	107,034	88,913	97,974	9,061				T35	108,863	**88,913**	T29	**107,034**	87,070
M25	111,077	89,815	100,446	10,631							T30	**111,077**	**89,815**
M26	114,097	92,519	103,308	10,789							T31	**114,097**	**92,519**
M27	114,212	93,666	103,939	10,273							T32-T33	**114,212**	**93,666**
M28	114,453	93,562	104,008	10,446							T34	**114,453**	**93,562**
M29	121,405	94,153	107,779	13,626	T19	121,855	**94,153**				T35	**121,405**	98,074
M30	123,483	101,477	112,480	11,003							T36-T37	**123,483**	**101,477**
M31	130,322	99,806	115,064	15,258	T20	**130,322**	**99,806**				–		
M32	133,250	106,524	119,887	13,363	T21	**133,250**	101,184				T38-T39	132,429	**106,524**
M33/MM4	132,190	110,259	121,225	10,966	T23	135,399	103,277				T40	**132,190**	**110,259**

Note. Values in bold correspond to the age of the event-deposits taken into account to estimate the ages of the margin events. When the ages of the event deposits likely to have been triggered by the same marginal event do not overlap, the least likely ages of the event-deposits are shown in italics and are not taken into account for the age of the margin-event (see main text for details).

over a distance of ~140 km (Zone B from Méduse to Karukera Basins). Thirteen M events promoted event deposits over a distance of ~100 km (Zone C, from Méduse to Désirade Basins). Eight B events were recorded in the Caravelle Half Graben and Désirade Basin over a distance of ~40 km. It is likely that all MM events that triggered exceptional thick HmTu deposits in several basins affected the margin over a large distance (at least the extent of zone A, 170 km); however, the CAS16-31PC is too short to confirm this.
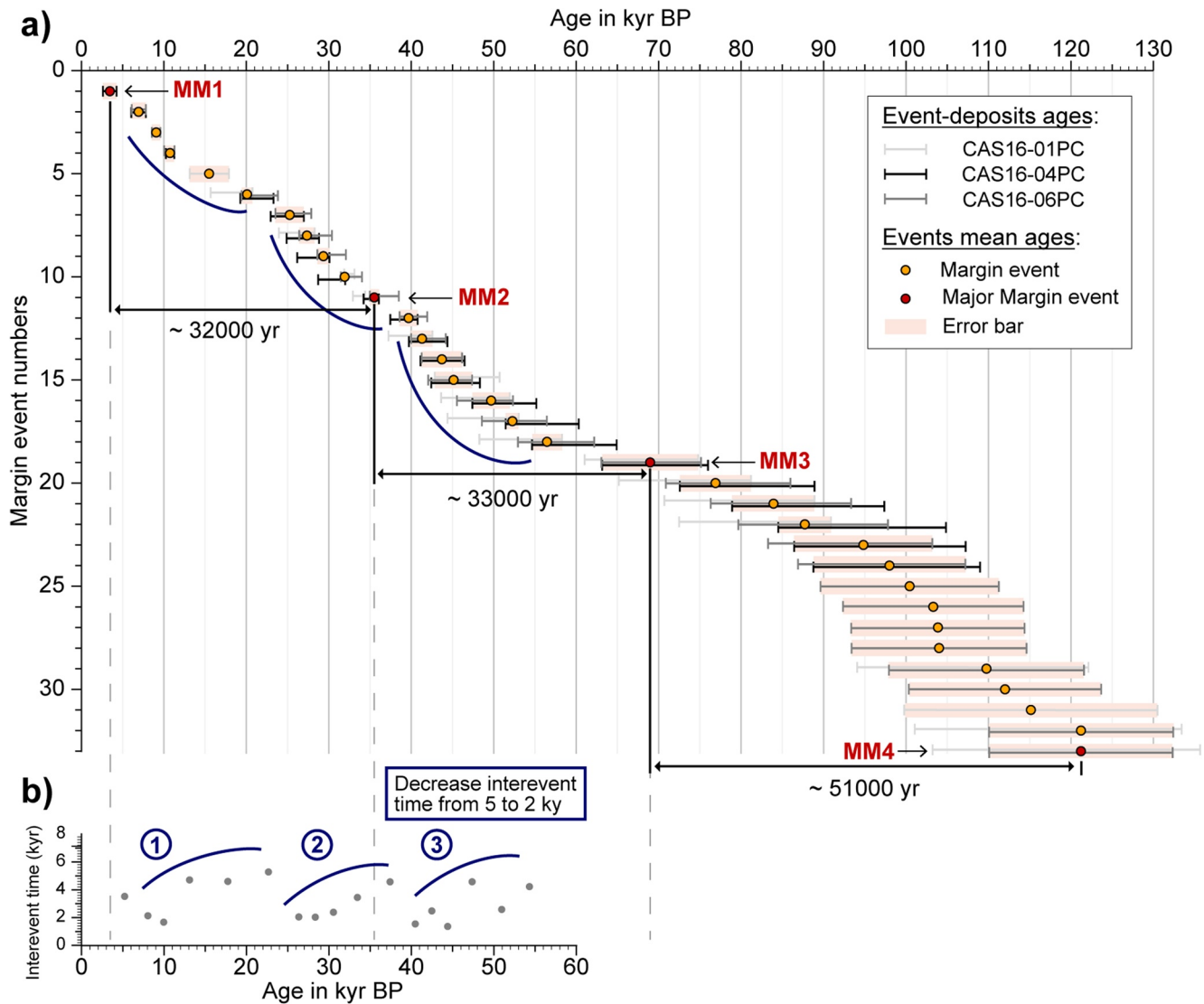
Figure 9. Ages of the margin events and inter-event times. (a) Age of the margin events obtained from synthetic age models of CAS16-01PC, CAS16-04PC, and CAS16-06PC, merging radiocarbon dates, biostratigraphic limit and MM events correlations. See more detail in Supplementary S7 of the Supporting Information S1. (b) Evolution of inter-event time over the last 60 Kyr.

5. Discussion

5.1. Origins of the Event Deposits

The Karukera Basin, Méduse Basin and Falmouth Half Graben are completely isolated basins. The sediment routing systems identified by Seibert et al. (2020) indicate that these basins are only fed by canyons restricted to local slopes (in Red, Figure 10). This is in agreement with the sediment analyses performed on the cores CAS16-01PC, -07PC and -14PC taken in those basins. The XRF data of these cores and the coarse grained fraction observations of the core CAS16-14PC indicate that the sediment record consists of calcite-rich and calcite-aragonite-rich turbidites (Figure 6), with open-sea organisms (planktonic foraminifera and pteropods; Supplementary S3 in Supporting Information S1) suggesting that the sediments may originate from the destabilization of local slopes. By contrast, the cores sampled in the Désirade Basin and Caravelle Half Graben (cores CAS16-04 and -06PC, respectively) are mostly composed of aragonite-rich turbidites (Figure 6) containing shallow carbonate platform organisms (e.g., Homotrematidea and Bryozoa; Supplementary S3 in Supporting Information S1), indicating either primary sources from the neighboring upslope shallow reef environment (Grande-Terre and Flandre Bank carbonate platforms) or remobilized material. Sediments can be exported from carbonate platforms, trapped
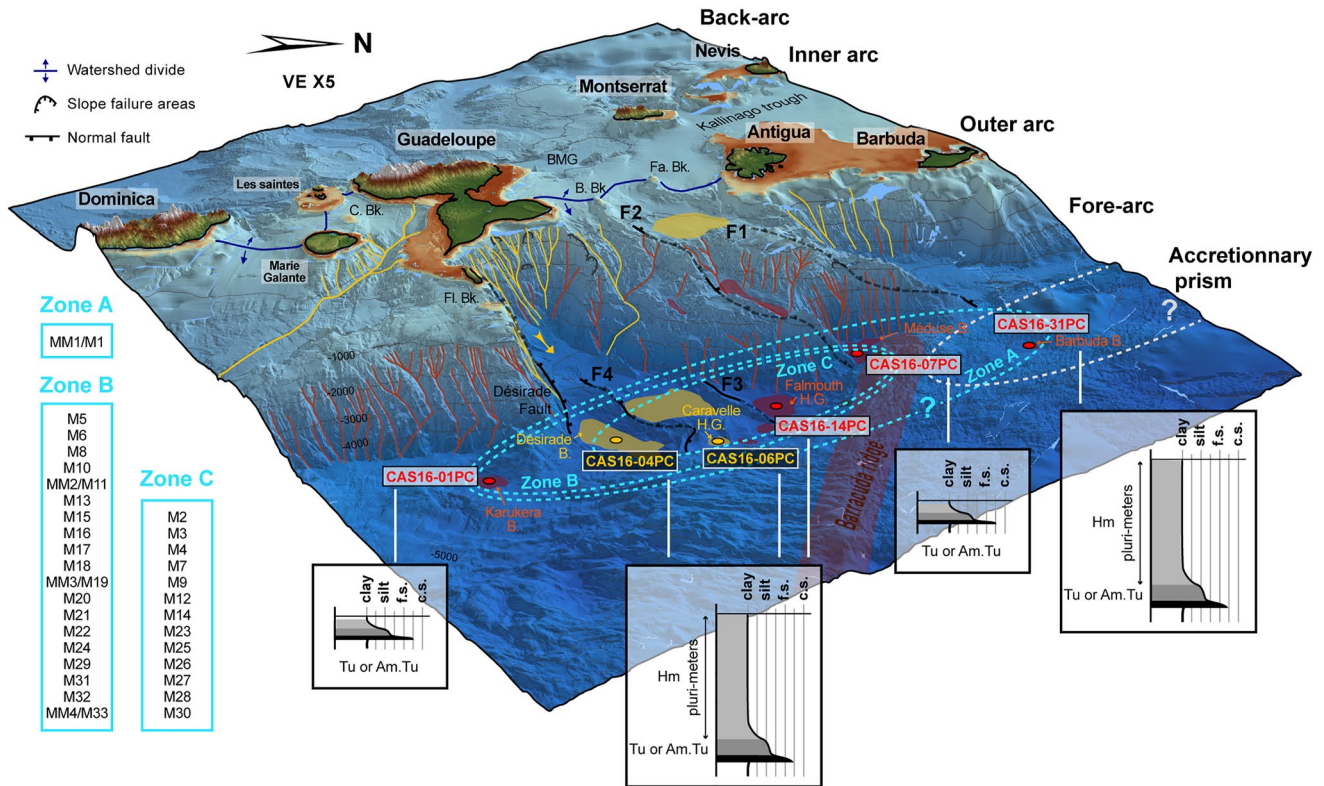
Figure 10. 3D map of the study area showing the main morphologic features, the core-to-core correlation area and sediment facies associated the MM1 event. Red lines: canyons confined in the slope; Yellow lines: canyons connected to the shallow area (mapped by Seibert et al. (2020)); Red area: isolated basins; Yellow areas: connected basins; Black lines: normal faults labeled F1 to F4 and the Désirade fault, dashed lines fault behind the reliefs (Feuillet et al., 2001); Light blue dashed circle: Extent of turbidite correlation across cores with the seismic events associated in the light blue rectangles on the left; Sedimentary facies of the Major Margin event: turbidites (Tu) or amalgamated turbidite (Am. Tu) in the Méduse and Karukera Basins and several-m-thick "Homogenite + turbidite" (Hm: Homogenite) in Désirade Trough basins; for the MM1 there is likely a correlation with HmTu in Barbuda Basin; C.Bk.: Colombian bank; Flandre Bk.: Flandre Bank; B.Bk.: Bertrand Bank; Fa. Bk.: Falmouth Bank; BMG: Bouillante-Montserrat Graben; B.: Basin; H.G.: Half Graben.

in canyon heads, along the edge of the carbonate platform (Puig et al., 2004; Stevens et al., 2014), and further mobilized by more energetic processes such as earthquakes (Mountjoy et al., 2018). The Désirade Basin and Caravelle Half Graben are fed through canyons (in Yellow, Figure 10), the heads of which are likely connected to the shallow carbonate platform (Seibert et al., 2020). In those basins, isolated uncorrelated event deposits or B event deposits that can be correlated with the two basins could have been triggered by earthquakes (local or regional), hurricanes, tsunami waves, or random slope failures of carbonate platforms. Whatever the nature of the event, its magnitude has likely exceeded those of historical events, for which we have no sedimentary record. The only possible source of event deposits found in other basins is earthquake shaking or isolated local slope failure when the event deposits are uncorrelated.

In all cores, we identified amalgamated turbidites (Figure 4). For some of them, we highlighted pulses of different contents (Table S3-1 in Supporting Information S1). Such deposits have been interpreted elsewhere as single deposits resulting from multiple synchronous slope failures, usually triggered by earthquakes (Migeon et al., 2017; Nakajima & Kanai, 2000; Van Daele et al., 2017). More recently, Howarth et al. (2021) have shown that the grain size pulses within the amalgamated turbidites may have preserved the 2016 Mw 7.8 Kaikōura earthquake ground motion. The exceptional stack of 10 amalgamated turbidites in core CAS16-07PC (Figure 4) suggests the occurrence of another major event in between M4 and M5. Two B-events promoted amalgamated turbidites in core CAS16-04PC (T27 and T31, Figure 6) and were likely earthquakes.

The exceptional up to 8-m thick homogenite deposits (Figures 4 and 6), sampled in the Désirade Trough sub-basins and Barbuda Basin, can be compared to those having been promoted by megathrust earthquakes in Japan (Kioka et al., 2019) including the Mw 9.1 Tohoku earthquake (McHugh et al., 2020). Homogenites have been observed in numerous marine and lacustrine environments and are commonly attributed to large earthquakes

in association with possible tsunamis (Beck et al., 2007; Chapron et al., 1999; Goldfinger et al., 2012; Kastens & Cita, 1981; McHugh et al., 2016, 2020; Mulder et al., 2009). Several mechanisms have been inferred to promote such depositional architectures. Some studies concur to show that such deposits result from fine-grained particle segregation by a long-wavelength oscillation of the water column (seiche effect), either promoted by the entering in the water of a huge amount of failed sediment (Mulder et al., 2009; Vermassen et al., 2023) or by tsunami waves (Beck, 2009). Others proposed that they result from the remobilization of the surficial sediment over a large area (Ashi et al., 2014; McHugh et al., 2016; Moernaut et al., 2017) induced by the ground motions (McHugh et al., 2020). Those sediments can further be transported to form thick homogenous deposits in deep depressions, as observed in the Japan Trench after the Tohoku earthquake (McHugh et al., 2016). The seiche effects or the seismic waves must be strong enough to dislodge the upper few centimeters of sediments. A link was proposed between the amplitude and duration of the ground motion and the thickness of the homogenites (McHugh et al., 2016).

5.2. Sources of the Earthquakes

Megathrust earthquake events surpassing the 1843 earthquake in magnitude or having different frequency content of ground motion are likely the cause of the MTD, regionally correlated HmTu and amalgamated turbidites, we have documented in the bathymetry and SBP profiles and in the sediment cores. No event deposit is found to correlate with this major 1843 historical event that promoted intensities between IX and X in the island near our sampling area. Such intensities imply acceleration larger than 0.3 g from the B3 law (Beauducel et al., 2011). This is larger than the measured or estimated peak-ground acceleration (PGA) thresholds for triggering a slope failure in subaqueous environments (0.1–0.2 g, d'Acremont et al., 2022; Dan et al., 2009; Noda et al., 2008), although Mountjoy et al. (2018) estimated a PGA threshold of ~0.38–0.44 g for canyon rim failure during the Kaikoura earthquake from direct observations made right after the earthquake. Several hypotheses could explain the absence of the 1843 earthquake deposit: (a) The surficial slope sedimentary layers may have been insufficient or too strong to be remobilized at the time of the earthquake. Older event deposits were however found in the Holocene period, and it is unlikely that either the sedimentation rate or the ability of the sedimentary layers covering the slope to fail vary over few millennia. (b) The magnitude of the earthquake may have been overestimated but even when considering the lowest estimation of intensities by Bernard and Lambert (1988), the PGA is still larger than 0.3 g. (c) The origin of 1843 is still debated and this earthquake may have been an intra-slab earthquake with higher frequency content of ground motion than interpolate megathrust earthquakes. From lacustrine sediment records, it was inferred that megathrust earthquakes in Chile are more likely to trigger subaquatic slope failures (Van Daele et al., 2019). (d) The volume of remobilized sediment may have been too small, mixed into the in situ hemipelagic sedimentation by bioturbation and difficult to identify with the data in hand. We found broken materials in the hemipelagic layers, and we cannot exclude that the sediments were transported instead of being gently settled. However, further investigations are needed to prove this.

A preferred explanation is that the HmTu deposits we sampled in the Lesser Antilles may result from surficial remobilization of the upper few centimeters of sediment due to earthquake-induced ground motion or seiche effect. It was proposed that the duration and the frequency content of the seismic ground motion at a site and thus the earthquake magnitude and not PGA could be the key factors to control the surficial sediment remobilization (Molenaar et al., 2019). It is thus possible that the magnitude threshold to promote an event deposit in the area is larger than that of the 1843 earthquake (Magnitude >8). In the Tohoku region, the magnitude threshold was estimated to be larger or equal to 8 (Molenaar et al., 2019). More recently, Ikehara et al. (2023) estimated that PGAs larger than 0.6 g are needed to remobilize the surficial sediments in this region. Moreover, the 1843 earthquake source was deep, probably in the mantle-wedge (Beauducel & Feuillet, 2012), and was associated with only a very small tsunami (Bernard & Lambert, 1988). The ground-motion- or seiche effect-induced stresses at the sediment-water interface may have been insufficient to remobilize the upper veneer of the surficial sediment. How and when an event deposit is triggered or not by a large earthquake is still not fully understood and remains controversial. The observations and measurements made immediately after major earthquakes were crucial to further improve our understanding in this domain. The Mw 7.1 Haiti 2010 (McHugh et al., 2011), Mw 9.1 Tohoku Japan 2011 (McHugh et al., 2016) and Mw 7.8 Kaikoura New Zealand 2016 (Howarth et al., 2021; Mountjoy et al., 2018) earthquakes promoted slope failure or remobilization of surficial sediments leading to a diversity of event deposits (MTD, turbidites, amalgamated turbidites, homogenites or a combination of both). Based on that finding, it is likely that the four MM events that promoted the HmTu were likely very large earthquakes

comparable to the Japan megathrust earthquakes, possibly associated with a large tsunami. Amalgamated and classical turbidites are associated with several meters thick homogenite deposits. This suggests both massive and multiple slope failures and surficial remobilization during large magnitude earthquakes.

The Lesser Antilles being a complex tectonic region, we cannot exclude however that ruptures on crustal faults in the overriding plate or in the slab at shallow or intermediate depths could promote earthquakes large enough to trigger slope failures in a large area. It is noteworthy, however, that no deposit is found in our sedimentary record in association with the largest historical Magnitude 6–7 class earthquakes on those faults. A large intermediate intraslab earthquake similar to the Mw7.4 November 2007 in Martinique would have been felt with intensities ranging between V and VI and had a PGA ranging between 0.015 and 0.068 g in our sampling area (Beauducel et al., 2011) whereas PGA lower than 0.05 g were estimated for Magnitude 6.3 earthquakes having occurred along the arc-parallel fault systems (16 March 1985 and 21 November 2004 earthquakes), 100 km away from our sampling site. Those PGAs are certainly too small to destabilize the slopes or remobilize the surficial sediment. The absence of event deposits associated with the 8 October 1974 M 7.4 earthquake that occurred between Antigua and Barbuda (Figure 1a), likely on the N50°E striking fault bounding the Antigua valley to the south, is surprising as intensities up to IX and PGA up to 0.7 g were inferred for this earthquake (Beauducel et al., 2011; Feuillet et al., 2011). Four 30 to 55 km long main faults of this family (F1 to F4) were mapped close to our sampling sites (Figures 1b and 10). By considering ruptures of the entire fault, the empirical relation of Wells and Coppersmith (1994) gives a maximum magnitude of ~7 on these crustal earthquakes (see detail in Supplementary S8 in Supporting Information S1). This magnitude is on the same order as that of the 1974 earthquake. A complete analysis of the PGA expected for rupture on such faults is presented in Supplementary S8 of the Supporting Information S1.

Although this analysis is approximate in nature, and a fuller analysis with physical property measurements is required for a more definitive test of sources, we conclude that the normal faults are unlikely to be capable of generating correlative deposits fully spanning the region between the southernmost and northernmost correlated cores in Zones A and B. On the basis of our PGA calculations, we cannot entirely exclude that event deposits correlated with the smaller zone C (13 out of 33 deposits) were promoted by the rupture of one of the F1 to F4 normal faults. However, the absence of event deposits related to historical earthquakes of larger magnitude (7.4) makes this hypothesis very unlikely. All the event deposits were triggered by earthquakes larger than all historical earthquakes, including the largest one in 1843. They were likely large magnitude interplate earthquakes that also ruptured the shallower part of the megathrust and were not restricted to the deeper part of the megathrust (as inferred for the 1946, 1839, and 1843 earthquakes Feuillet et al., 2011; Weil-Accardo et al., 2016).

5.3. Seismic Super-Cycle and Seismic Segmentation?

Figure 9 highlights three long-term cyclic patterns of inter-events over the last ~60 Kyr. Assuming the paleo-earthquake record is complete, those cycles are 15–20 Kyr long and there is a progressive shortening of inter-event times from ~5 down to ~2 Kyr in between two consecutive cycles (Figure 9b). Although the exact interval duration should be taken with caution given that the error bar of the modeled ages may exceed a couple of Kyr, the trend showing a decrease in the inter-event time is striking. It is noteworthy that the MM3 and MM2 events are coeval to the onset of the third and second cycles and that the MM1 event seems to mark the end of the youngest cycle. This behavior contrasts with the four behaviors listed by Philibosian and Meltzner (2020) in their review of paleoseismological records: (a) Quasi-periodic with similar ruptures, that is, homogeneous recurrence interval, rupture location, and magnitude, (b) Clustered with similar ruptures, that is, heterogeneous recurrence intervals but homogeneous rupture location and magnitude, (c) Clustered with complementary ruptures or rupture cascades, and (d) Superimposed cycles. Although we cannot estimate the magnitude of the palaeo-earthquakes on the basis of our correlation distances only, the nature of our deposits suggests at least two classes of events: the MM events and other likely smaller events. In addition, our data set reveals variable inter-event times. Overall, this is incompatible with the quasi-periodic behavior of the megathrust or clustered earthquakes with similar ruptures. Instead, we may have evidenced supercycles with a clustered behavior as well as superimposed cycles over the last ~60 Kyr. The MM events, which are likely megathrust earthquakes of exceptional magnitude, partly outline the beginning or the end of a supercycle (Figure 9), as observed in Sumatra (Sieh et al., 2008) or partly in Cascadia (Goldfinger et al., 2013).

Although our study is limited to the northernmost part of the arc, it is noteworthy that most of the M events and all MM events, except for MM1, are limited to zone B (Figure 10). This zone is in front of Guadeloupe, in between the Tiburon and Barracuda ridges, and corresponds to the extent of the 1843 rupture area (Figure 11; Feuillet
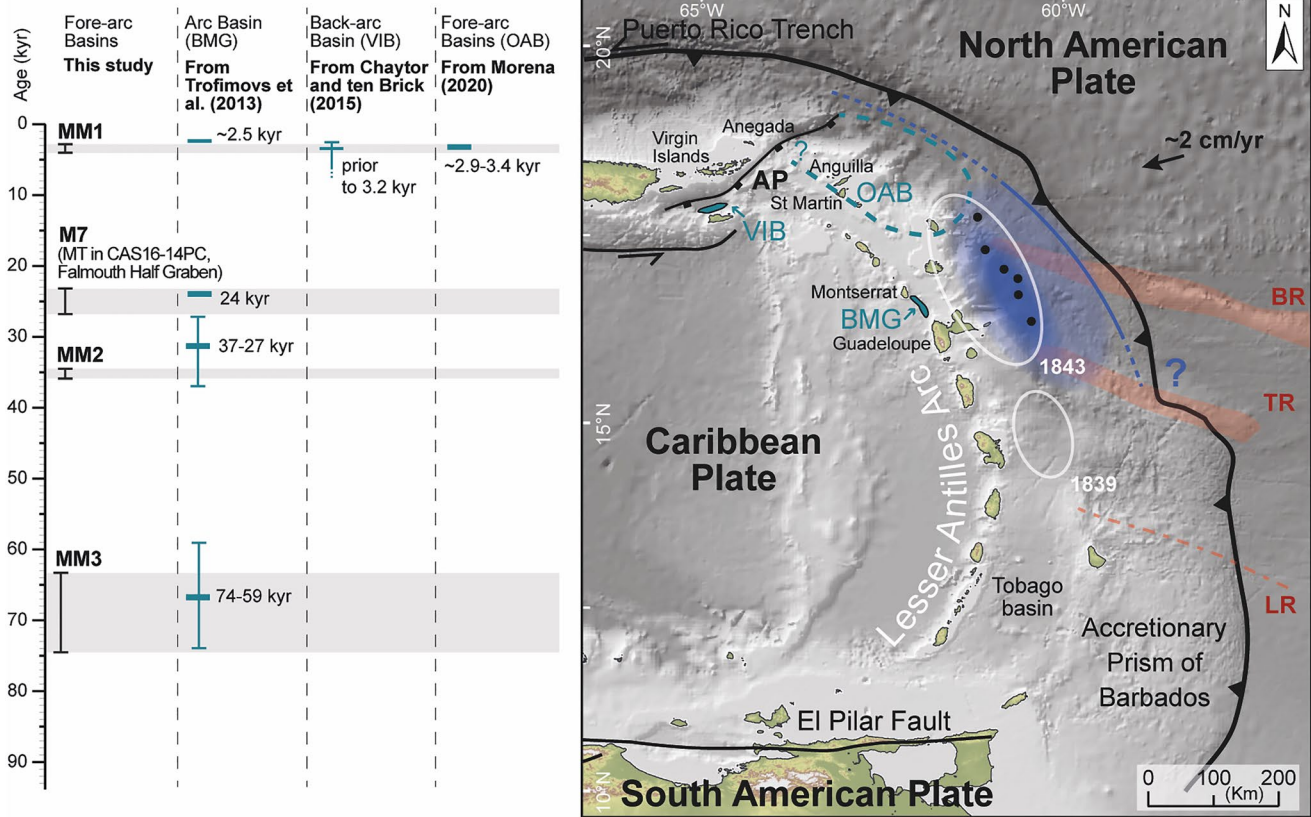
Figure 11. Major Margin events. On the left, diagram comparing the dates of the Major Margin events of this study with events described in the literature: the bioclastic-content turbidites described by Trofimovs et al. (2013) in Bouillante-Montserrat Graben, Morena (2020) offshore Anguilla Island, and with the homogenite described by Chaytor and ten Brink (2015) (called unifit in their paper) in the Virgin Island Basin; On the right, map of the Lesser Antilles subduction zone with the Barbados accretionary prism deformed by subducting ridges, Barracuda (BR) and Tiburon (TR) ridges in red areas and St Lucia ridge (LR) in red dashed line (Laigle et al., 2013 and references therein); Colored dots: locations of cores CAS16-01PC, CAS16-04PC, CAS16-06PC, and CAS31PC according to the color on the diagram; White circles: outline of the probable rupture zones of the 1843 and 1839 earthquakes (Feuillet et al., 2011); blue area: probable rupture area of the Major Margin events, maybe extending along the hatched area, curved blue line: length of the plate interface which could have broken during the MM1 if the correlation with the unifit observed in the Virgin Island Basin is confirmed; BMG: Bouillante Montserrat Graben; AP: Anegada Passage.

et al., 2011). On the other hand, the core CAS16-31PC, which is located northward of the Barracuda Ridge in a basin isolated from the margin (Seibert et al., 2020), shows a different event record (i.e., 3 HmTu and six turbidites in only 7 Kyr; Figures 4 and 6). Subduction of aseismic ridges, such as the Tiburon and Barracuda ridges, has long been inferred to impact the seismic potential of the megathrust along various subduction zones (Bassett & Watts, 2015; McCann & Sykes, 1984; Meltzner et al., 2012; van Rijsingen et al., 2018; Wallace et al., 2009; Wang & Bilek, 2014), as they may act as barriers preventing rupture propagation. The most recent MM1 event, which occurred between 2.5 and 3.5 Kyr, was likely also recorded in the Barbuda Basin, located northward of the Barracuda Ridge, beyond zone B (Figure 10). This would likely imply a larger magnitude earthquake that may have broken several asperities (Avouac, 2015; Kaneko et al., 2010). This is what is observed when an earthquake becomes a mega-earthquake. For instance, the 2004 Sumatra earthquake ruptured several asperities of the Sunda megathrust (Chlieh et al., 2007). This was also observed during the Maule 2010 earthquake in Chile (Chlieh et al., 2007; Lorito et al., 2011; Vigny et al., 2011).

A complementary paleoseismological study performed in the northern part of the arc revealed a turbidite deposit off the Anguilla Bank, coeval to the MM1 event (~2.9–3.4 Kyr, Morena, 2020). Northwards, in the Virgin Islands Basin, Chaytor and ten Brink (2015) sampled a homogenite, for which dating indicated an age of 3,200 years (Figure 11). Westwards of our study area, in the Bouillante-Montserrat Graben (in between Montserrat and Guadeloupe islands; Figure 11), Trofimovs et al. (2013) identified and characterized several mass flow deposits. While most of them were promoted by the collapse of the volcanic dome of Montserrat, four were exclusively made by bioclastic particles and resulted from carbonate platform collapses. These events have been dated to

~2.5 Kyr, ~24 Kyr, 27–37 Kyr, and 59–74 Kyr (Trofimovs et al., 2013; Figure 11). The ages of three of these events strikingly coincide with those of our MM deposits, and the youngest is coeval with the MM1 event identified in this study (Figure 11). Coeval 2.5–3.5-Kyr-old sedimentary events can thus be found in the fore-arc over a large distance but also farther from the trench along the arc or even in the Virgin Island basins. Therefore, they may have been deposited during a single large seismic event that affected all the margins between Guadeloupe and the Virgin Islands, over a distance of several hundreds of kilometers. If attested, this would imply that the MM events are massive multi-asperity ruptures with rupture lengths comparable to those of the most recent megathrust earthquakes in Chile (2010), and Japan (2011) (Moreno et al., 2010; Ozawa et al., 2011).

Alternately, those layers may have been deposited over a short period of time, as a result of a sequence of smaller and adjacent ruptures, similar to what happened in the middle of the 19th century with the occurrence 4 years apart from the 1839 and 1843 earthquakes. This has also been documented from sediment records along the Chile margin (Wils et al., 2020). For instance, the 25 December Mw 9.1 earthquake was followed a few months later, on 28 March 2005, by another megathrust Mw 8.7 earthquake that ruptured a segment of the Sunda megathrust situated immediately to the south (Briggs et al., 2006). The fact that those MM events may have triggered massive carbonate platform collapses along the volcanic arc, far from the trench in the Bouillante-Montserrat Graben, may be however in favor of a large rupture of the whole plate interface with a deep downdip limit very close to the active volcanic arc, rather than a sequence of smaller ruptures. This downdip limit is inferred to lie at a depth of 60 km (Bie et al., 2020; Laigle et al., 2013; Philibosian et al., 2022; Weil-Accardo et al., 2016). It was shown that the 2004 Sumatra or 2011 Japan megathrust earthquakes ruptured a large part of the plate interface, from the mantle wedge to the accretionary wedge front (Fujiwara et al., 2011; Gulick et al., 2011). North of the Barracuda ridge, we collected three thick HmTu deposits and 5 turbidites in the Barbuda Basin in the last 7 Kyr. Because the basin is completely isolated, the only possible sources for these event deposits are earthquakes. With only one core in this area, we cannot confirm the spatial extent of these event deposits. Their nature (HmTu) however suggests that two of them (in addition to the younger Hm1T1 deposit) were also triggered by M or MM events: the Hm2T7 (about 6 Kyr BP) and Hm3T9 (about 7.3 Kyr) (Figure 7). We infer that each of those was promoted by a large earthquake on a section of the megathrust located north of the Barracuda ridge maybe extending over the whole northern part of the arc (up to the Anegada Passage, Figure 11). Seven cores were taken in this area and their analysis, in progress (Morena et al., 2022), is needed to confirm this hypothesis. It is noteworthy that large pre-columbian overwashed sand deposits were found in Anegada (British Virgin Islands, Atwater et al., 2017) and in several other coastal lagoons and ponds in Anguilla and Saint Martin (Biguenet et al., 2021, 2022). Tsunami models suggest that these deposits were triggered by a large earthquake in the northern portion of the megathrust (Cordrie et al., 2022). Overall, this suggests that this portion of the megathrust may rupture more often than the segment located south of the Barracuda ridge.

6. Conclusions

This study proposes the first sub-aqueous paleoseismological reconstruction for the last 120 Kyr in the Lesser Antilles arc, based on sedimentological and stratigraphic analyzes of six piston cores located in deep fore-arc basins confined between the arc basement and the accretionary wedge. Thirty-three margin-scale events have been dated and correlated with the up to 170 km extent covered by these fore-arc basins based on the identification of turbidites. From the turbidite characteristics and their spatial extent, earthquakes are considered the most likely trigger for the synchronous events. Based on the broad correlation area and PGA estimates, we propose that the causative earthquakes are large-magnitude subduction earthquakes. In particular, we found exceptional thick homogenites that were likely promoted by extended remobilization of the upper veneers of sediments by earthquake ground shaking, as observed along the Japan trench after the Tohoku Oki 2011 earthquake.

From the radiocarbon ages and variations of planktonic foraminifera content, three 15–25 Kyr-long supercycles could be identified, characterized by a progressive shortening of the recurrence interval for subsequent events in a single cycle from 5 to 2 Kyrs. The four Major Margin (MM) events we observed are dated around ~3.3, 35, 70, and 120 Kyr and triggered the thick turbidite + homogenite (HmTu) deposits we identified offshore Guadeloupe island. Moreover, coeval event deposits were found in the arc (carbonate platform failure deposits in the Bouillante-Montserrat Graben) and in the back-arc (homogenite in the Virgin Island Basin). This suggests that those MM events are probably earthquake ruptures extending over several hundred kilometers and along deeper portions of the megathrust. This seems to be the characteristic of the most recent large megathrust earthquakes in Sumatra and Japan (Tohoku).

The spatial extent of the deposits likely revealed a segmentation of the megathrust. We showed contrasting sedimentary records in basins located southward and northward of the Barracuda ridge. This suggests that those aseismic ridges may act as barriers limiting the propagation of earthquake ruptures and that the plate interface is segmented. The MM events may have ruptured all the asperities leading to much larger magnitude earthquakes. Given the uncertainties on the radiocarbon dating, we cannot exclude a cluster of smaller ruptures closely spaced in time (decades to few centuries). However, the event deposits found coeval in the arc and back-arc favor the former hypothesis. No trace of historical large intraplate earthquakes or earthquakes on crustal faults was found in our sedimentary record, suggesting that the event deposits we identified were triggered by earthquakes with magnitudes surpassing that of the largest 8 February 1843 event. We sampled more event deposits in the Barbuda Basin, north of the Barracuda ridge, suggesting that the northern segment may be more prone to promote large earthquakes. It is also along this segment that large pre-columbian overwashed deposits were found. The ongoing analysis of seven cores sampled in this area will be crucial to confirm this.

Data Availability Statement

All geophysical data (bathymetry, backscatter and sub-bottom profiles) are stored on the SISMER Database (Feuillet, 2016; https://campagnes.flotteoceanographique.fr/campagnes/16001800/fr/). The sedimentary cores are on the repository of the Museum National d'Histoire Naturelle. The data are accessible using the following link and with the inventory name GS-MNHN followed by the core number: https://science.mnhn.fr/institution/mnhn/collection/gs/item/search/form. The data obtained on the sedimentary cores are stored on SEANOE: CAS16-01PC (Seibert et al., 2023f), CAS16-03PC (Seibert et al., 2023a), CAS16-04PC (Seibert et al., 2023d), CAS16-06PC (Seibert et al., 2023c), CAS16-07PC (Seibert et al., 2023e), CAS16-14PC (Seibert et al., 2023a), and CAS16-31PC (Seibert et al., 2023b).

References

Adams, J. (1990). Paleoseismicity of the Cascadia subduction zone: Evidence from turbidites off the Oregon-Washington margin. *Tectonics*, *9*(4), 569–583. https://doi.org/10.1029/tc009i004p00569

Ammon, C. J., Lay, T., Kanamori, H., & Cleveland, M. (2011). A rupture model of the 2011 off the Pacific coast of Tohoku earthquake. *Earth Planets and Space*, *63*(7), 33–696. https://doi.org/10.5047/eps.2011.05.015

Ashi, J., Sawada, R., Omura, A., & Ikehara, K. (2014). Accumulation of an earthquake-induced extremely turbid layer in a terminal basin of the Nankai accretionary prism. *Earth Planets and Space*, *66*(1), 1–9. https://doi.org/10.1186/1880-5981-66-51

Atwater, B. F., ten Brink, U. S., Cescon, A. L., Feuillet, N., Fuentes, Z., Halley, R. B., et al. (2017). Extreme waves in the British Virgin Islands during the last centuries before 1500 CE. *Geosphere*, *13*(2), 301–368. https://doi.org/10.1130/ges01356.1

Avouac, J. P. (2015). From geodetic imaging of seismic and aseismic fault slip to dynamic modeling of the seismic cycle. *Annual Review of Earth and Planetary Sciences*, *43*(1), 233–271. https://doi.org/10.1146/annurev-earth-060614-105302

Babonneau, N., Cattaneo, A., Ratzov, G., Déverchère, J., Yelles-Chaouche, A., Lateb, T., & Bachir, R. S. (2017). Turbidite chronostratigraphy off Algiers, central Algerian margin: A key for reconstructing Holocene paleo-earthquake cycles. *Marine Geology*, *384*, 63–80. https://doi.org/10.1016/j.margeo.2016.10.017

Bassett, D., & Watts, A. B. (2015). Gravity anomalies, crustal structure, and seismicity at subduction zones: 2. Interrelationships between fore-arc structure and seismogenic behavior. *Geochemistry, Geophysics, Geosystems*, *16*(5), 1541–1576. https://doi.org/10.1002/2014gc005685

Bazin, S., Feuillet, N., Duclos, C., Crawford, W., Nercessian, A., Bengoubou-Valérius, M., et al. (2010). The 2004–2005 Les Saintes (French West Indies) seismic aftershock sequence observed with ocean bottom seismometers. *Tectonophysics*, *489*(1–4), 91–103. https://doi.org/10.1016/j.tecto.2010.04.005

Beauducel, F., Bazin, S., Bengoubou-Valérius, M., Bouin, M.-P., Bosson, A., Anténor-Habazac, C., et al. (2011). Empirical model for rapid macroseismic intensities prediction in Guadeloupe and Martinique. *Comptes Rendus Geoscience*, *343*(11–12), 717–728. https://doi.org/10.1016/j.crte.2011.09.004

Beauducel, F., & Feuillet, N. (2012). The great 1843 earthquake in the Lesser Antilles arc. In *AGU fall meeting abstracts* (Vol. 2012, pp. T41A–T2558).

Beck, C. (2009). Late Quaternary lacustrine paleo-seismic archives in north-western alps: Examples of earthquake-origin assessment of sedimentary disturbances. *Earth-Science Reviews*, *96*(4), 327–344. https://doi.org/10.1016/j.earscirev.2009.07.005

Beck, C., Mercier de Lépinay, B., Schneider, J.-L., Cremer, M., Çağatay, N., Wendenbaum, E., et al. (2007). Late Quaternary coseismic sedimentation in the Sea of Marmara's deep basins. *Sedimentary Geology*, *199*(1–2), 65–89. https://doi.org/10.1016/j.sedgeo.2005.12.031

Beck, C., Reyss, J.-L., Leclerc, F., Moreno, E., Feuillet, N., Barrier, L., et al. (2012). Identification of deep subaqueous co-seismic scarps through specific coeval sedimentation in Lesser Antilles: Implication for seismic hazard. *Natural Hazards and Earth System Sciences*, *12*(5), 1755–1767. https://doi.org/10.5194/nhess-12-1755-2012

Bernard, P., & Lambert, J. (1988). Subduction and seismic hazard in the northern Lesser Antilles: Revision of the historical seismicity. *Bulletin of the Seismological Society of America*, *78*(6), 1965–1983.

Bie, L., Rietbrock, A., Hicks, S., Allen, R., Blundy, J., Clouard, V., et al. (2020). Along-arc heterogeneity in local seismicity across the Lesser Antilles subduction zone from a dense ocean-bottom seismometer network. *Seismological Research Letters*, *91*(1), 237–247. https://doi.org/10.1785/0220190147

Bieber, A., St-Onge, G., Feuillet, N., Carlut, J., Moreno, E., & Michel, E. (2021). Regional chronostratigraphy in the eastern Lesser Antilles quaternary fore-arc and accretionary wedge sediments: Relative paleointensity, oxygen isotopes and reversals. *Quaternary Geochronology*, *65*, 101179. https://doi.org/10.1016/j.quageo.2021.101179

Biguenet, M., Chaumillon, E., Sabatier, P., Paris, R., Vacher, P., & Feuillet, N. (2022). Distinguishing between tsunamis and hurricanes in the same sedimentary record using X-ray tomography. *Marine Geology*, *450*, 106864. https://doi.org/10.1016/j.margeo.2022.106864

Biguenet, M., Sabatier, P., Chaumillon, E., Chagué, C., Arnaud, F., Jorissen, F., et al. (2021). A 1600 year-long sedimentary record of tsunamis and hurricanes in the Lesser Antilles (Scrub Island, Anguilla). *Sedimentary Geology*, *412*, 105806. https://doi.org/10.1016/j.sedgeo.2020.105806

Boucard, M., Marcaillou, B., Lebrun, J. F., Laurencin, M., Klingelhoefer, F., Laigle, M., et al. (2021). Paleogene V-shaped basins and Neogene subsidence of the northern Lesser Antilles forearc. *Tectonics*, *40*(3), e2020TC006524. https://doi.org/10.1029/2020tc006524

Bouma, A. H. (1962). Sedimentology of some flysch deposits. *Agraphic Approach to Facies Interpretation*, 168.

Bouysse, P., & Westercamp, D. (1990). Subduction of Atlantic aseismic ridges and Late Cenozoic evolution of the Lesser Antilles island arc. *Tectonophysics*, *175*(4), 349–380. https://doi.org/10.1016/0040-1951(90)90180-g

Briggs, R. W., Sieh, K., Meltzner, A. J., Natawidjaja, D., Galetzka, J., Suwargadi, B., et al. (2006). Deformation and slip along the Sunda megathrust in the great 2005 Nias-Simeulue earthquake. *Science*, *311*(5769), 1897–1901. https://doi.org/10.1126/science.1122602

Bronk Ramsey, C. (2008). Deposition models for chronological records. *Quaternary Science Reviews*, *27*(1–2), 42–60. https://doi.org/10.1016/j.quascirev.2007.01.019

Bronk Ramsey, C. (2009). Bayesian analysis of radiocarbon dates. *Radiocarbon*, *51*(1), 337–360. https://doi.org/10.1017/s0033822200033865

Bronk Ramsey, C., & Lee, S. (2013). Recent and planned developments of the program OxCal. *Radiocarbon*, *55*(2–3), 720–730. https://doi.org/10.2458/azu_js_rc.55.16215

Brunet, M., Le Friant, A., Boudon, G., Lafuerza, S., Talling, P., Hornbach, M., et al., (2016). Composition, geometry, and emplacement dynamics of a large volcanic island landslide offshore Martinique: From volcano flank-collapse to seafloor sediment failure? Submarine landslides offshore Martinique. *Geochemistry, Geophysics, Geosystems*, *17*(3), 699–724. https://doi.org/10.1002/2015gc006034

Chapron, E., Beck, C., Pourchet, M., & Deconinck, J.-F. (1999). 1822 earthquake-triggered homogenite in Lake Le Bourget (NW Alps). *Terra Nova*, *11*(2–3), 7–92. https://doi.org/10.1046/j.1365-3121.1999.00230.x

Chaytor, J. D., & ten Brink, U. S. (2015). Event sedimentation in low-latitude deep-water carbonate basins, Anegada passage, northeast Caribbean. *Basin Research*, *27*(3), 310–335. https://doi.org/10.1111/bre.12076

Chlieh, M., Avouac, J. P., Hjorleifsdottir, V., Song, T. R. A., Ji, C., Sieh, K., et al. (2007). Coseismic slip and afterslip of the great Mw 9.15 Sumatra–Andaman earthquake of 2004. *Bulletin of the Seismological Society of America*, *97*(1A), S152–S173. https://doi.org/10.1785/0120050631

Cordrie, L., Feuillet, N., Gailler, A., Biguenet, M., Chaumillon, E., & Sabatier, P. (2022). A megathrust earthquake as source of a pre-Colombian tsunami in Lesser Antilles: Insight from sediment deposits and tsunami modeling. *Earth-Science Reviews*, *228*, 104018. https://doi.org/10.1016/j.earscirev.2022.104018

Croudace, I. W., Rindby, A., & Rothwell, R. G. (2006). ITRAX: Description and evaluation of a new multifunction X-ray core scanner. *Geological Society, London, Special Publications*, *267*(1), 51–63. https://doi.org/10.1144/gsl.sp.2006.267.01.04

d'Acremont, E., Lafuerza, S., Rabaute, A., Lafosse, M., Castelot, M. J., Gorini, C., et al. (2022). Distribution and origin of submarine landslides in the active margin of the southern Alboran Sea (Western Mediterranean Sea). *Marine Geology*, *445*, 106739. https://doi.org/10.1016/j.margeo.2022.106739

Dan, G., Sultan, N., Savoye, B., Deverchere, J., & Yelles, K. (2009). Quantifying the role of sandy–silty sediments in generating slope failures during earthquakes: Example from the Algerian margin. *International Journal of Earth Sciences*, *98*(4), 769–789. https://doi.org/10.1007/s00531-008-0373-5

DeMets, C., Jansma, P. E., Mattioli, G. S., Dixon, T. H., Farina, F., Bilham, R., et al. (2000). GPS geodetic constraints on Caribbean-North America plate motion. *Geophysical Research Letters*, *27*(3), 437–440. https://doi.org/10.1029/1999gl005436

Deville, E., Mascle, A., Callec, Y., Huyghe, P., Lallemant, S., Lerat, O., et al. (2015). Tectonics and sedimentation interactions in the east Caribbean subduction zone: An overview from the Orinoco delta and the Barbados accretionary prism. *Marine and Petroleum Geology*, *64*, 76–103. https://doi.org/10.1016/j.marpetgeo.2014.12.015

Dorel, J. (1981). Seismicity and seismic gap in the Lesser Antilles arc and earthquake hazard in Guadeloupe. *Geophysical Journal International*, *67*(3), 679–695. https://doi.org/10.1111/j.1365-246x.1981.tb06947.x

Dutkiewicz, A., & Müller, D. (2022). The history of Cenozoic carbonate flux in the Atlantic Ocean constrained by multiple regional carbonate compensation depth reconstruction. *Geochemistry, Geophysics, Geosystems*, *23*(11), e2022GC0106667. https://doi.org/10.1029/2022gc010667

Ericson, D. B., & Wollin, G. (1956). Correlation of six cores from the equatorial Atlantic and the Caribbean. *Deep Sea Research*, *3*(2), 104–125. https://doi.org/10.1016/0146-6313(56)90089-2

Feuillard, M. (1985). *Macrosismicité de la Guadeloupe et de la Martinique*. Observatoire volcanologique de la Soufrière. (Guadeloupe).

Feuillet, N. (2016). CASEIS cruise, RV Pourquoi pas? https://doi.org/10.17600/16001800

Feuillet, N., Beauducel, F., & Tapponnier, P. (2011). Tectonic context of moderate to large historical earthquakes in the Lesser Antilles and mechanical coupling with volcanoes. *Journal of Geophysical Research*, *116*(B10), B10308. https://doi.org/10.1029/2011jb008443

Feuillet, N., Leclerc, F., Tapponnier, P., Beauducel, F., Boudon, G., Le Friant, A., et al. (2010). Active faulting induced by slip partitioning in Montserrat and link with volcanic activity: New insights from the 2009 GWADASEIS marine cruise data. *Geophysical Research Letters*, *37*(19), L00E15. https://doi.org/10.1029/2010gl042556

Feuillet, N., Manighetti, I., & Tapponnier, P. (2001). Extension active perpendiculaire à la subduction dans l'arc des Petites Antilles (Guadeloupe, Antilles françaises). *Comptes Rendus de l'Academie des Sciences—Series IIA: Earth and Planetary Science*, *333*(9), 583–590. https://doi.org/10.1016/s1251-8050(01)01543-9

Feuillet, N., Manighetti, I., Tapponnier, P., & Jacques, E. (2002). Arc parallel extension and localization of volcanic complexes in Guadeloupe, Lesser Antilles. *Journal of Geophysical Research*, *107*(B12), 2331. https://doi.org/10.1029/2001jb000308

Feuillet, N., Tapponnier, P., Manighetti, I., Villemant, B., & King, G. C. P. (2004). Differential uplift and tilt of Pleistocene reef platforms and Quaternary slip rate on the Morne-Piton normal fault (Guadeloupe, French West Indies). *Journal of Geophysical Research*, *109*(B2), B02404. https://doi.org/10.1029/2003jb002496

Fujiwara, T., Kodaira, S., No, T., Kaiho, Y., Takahashi, N., & Kaneda, Y. (2011). The 2011 Tohoku-Oki earthquake: Displacement reaching the trench axis. *Science*, *334*(6060), 1240. https://doi.org/10.1126/science.1211554

Goldfinger, C., Ikeda, Y., Yeats, R. S., & Ren, J. (2013). Superquakes and supercycles. *Seismological Research Letters*, *84*(1), 24–32. https://doi.org/10.1785/0220110135

Goldfinger, C., Nelson, C. H., & Johnson, J. E. (2003). Deep-water turbidites as Holocene earthquake proxies: The Cascadia subduction zone and northern San Andreas fault systems. *Annals of Geophysics*, *46*(5).

Goldfinger, C., Nelson, C. H., Morey, A., Johnson, J. E., Gutierrez-Pastor, J., Eriksson, A. T., et al. (2012). *Turbidite event history: Methods and implications for Holocene paleoseismicity of the Cascadia subduction zone* (p. 18464). USGS Professional Paper 1661-F. U.S. Geological Survey.

Gràcia, E., Vizcaino, A., Escutia, C., Asioli, A., Rodés, Á., Pallàs, R., et al. (2010). Holocene earthquake record offshore Portugal (SW Iberia): Testing turbidite paleoseismology in a slow-convergence margin. *Quaternary Science Reviews*, *29*(9–10), 1156–1172. https://doi.org/10.1016/j.quascirev.2010.01.010

Gulick, S. P. S., Austin, J. A., Jr., McNeill, L. C., Bangs, N. L. B., Martin, K. M., Henstock, T. J., et al. (2011). Updip rupture of the 2004 Sumatra earthquake extended by thick indurated sediments. *Nature Geoscience*, *4*(7), 453–456. https://doi.org/10.1038/ngeo1176

Heaton, T., Köhler, P., Butzin, M., Bard, E., Reimer, R., Austin, W., et al. (2020). Marine20—The marine radiocarbon age calibration curve (0–55,000 cal BP). *Radiocarbon*, 62.

Heezen, B. C., & Ewing, W. M. (1952). Turbidity currents and submarine slumps, and the 1929 Grand Banks [Newfoundland] earthquake. *American Journal of Science*, *250*(12), 849–873. https://doi.org/10.2475/ajs.250.12.849

Hough, S. E. (2013). Spatial variability of "Did You Feel It?" Intensity data: Insights into sampling biases in historical earthquake intensity distributions. *Bulletin of the Seismological Society of America*, *103*(5), 2767–2781. https://doi.org/10.1785/0120120285

Howarth, J. D., Orpin, A. R., Kaneko, Y., Strachan, L. J., Nodder, S. D., Mountjoy, J. J., et al. (2021). Calibrating the marine turbidite palaeoseismometer using the 2016 Kaikōura earthquake. *Nature Geoscience*, *14*(3), 161–167. https://doi.org/10.1038/s41561-021-00692-6

Ikehara, K., Usami, K., & Kanamatsu, T. (2023). How large peak ground acceleration by large earthquakes could generate turbidity currents along the slope of northern Japan Trench. *Progress in Earth and Planetary Science*, *10*(1), 8. https://doi.org/10.1186/s40645-023-00540-8

Kaneko, Y., Avouac, J. P., & Lapusta, N. (2010). Towards inferring earthquake patterns from geodetic observations of interseismic coupling. *Nature Geoscience*, *3*(5), 363–369. https://doi.org/10.1038/ngeo843

Kastens, K. A., & Cita, M. B. (1981). Tsunami-induced sediment transport in the abyssal Mediterranean Sea. *GSA Bulletin*, *92*(11), 845–857. https://doi.org/10.1130/0016-7606(1981)92<845:tstita>2.0.co;2

Kioka, A., Schwestermann, T., Moernaut, J., Ikehara, K., Kanamatsu, T., Eglinton, T. I., & Strasser, M. (2019). Event stratigraphy in a hadal oceanic trench: The Japan trench as sedimentary archive recording recurrent giant subduction zone earthquakes and their role in organic carbon export to the deep sea. *Frontiers in Earth Science*, *7*, 319. https://doi.org/10.3389/feart.2019.00319

Laigle, M., Becel, A., de Voogd, B., Sachpazi, M., Bayrakci, G., Lebrun, J.-F., & Evain, M. (2013). Along arc segmentation and interaction of subducting ridges with the Lesser Antilles subduction forearc crust revealed by MCS imaging. *Tectonophysics*, *603*, 32–54. https://doi.org/10.1016/j.tecto.2013.05.028

Laurencin, M., Marcaillou, B., Graindorge, D., Lebrun, J. F., Klingelhoefer, F., Boucard, M., et al. (2019). The bunce fault and strain partitioning in the northern Lesser Antilles. *Geophysical Research Letters*, *46*(16), 9573–9582. https://doi.org/10.1029/2019gl083490

Lay, T., Kanamori, H., Ammon, C. J., Nettles, M., Ward, S. N., Aster, R., et al. (2005). The great Sumatra-Andaman earthquake of 26 December 2004. *Science*, *308*(5725), 1127–1133. https://doi.org/10.1126/science.1112250

Leclerc, F., Feuillet, N., & Deplus, C. (2016). Interactions between active faulting, volcanism, and sedimentary processes at an island arc: Insights from Les Saintes channel, Lesser Antilles arc. *Geochemistry, Geophysics, Geosystems*, *17*(7), 2781–2802. https://doi.org/10.1002/2016gc006337

Le Friant, A., Lock, E. J., Hart, M. B., Boudon, G., Sparks, R. S. J., Leng, M. J., et al. (2008). Late Pleistocene tephrochronology of marine sediments adjacent to Montserrat, Lesser Antilles volcanic arc. *Journal of the Geological Society*, *165*(1), 279–289. https://doi.org/10.1144/0016-76492007-019

Lorito, S., Romano, F., Atzori, S., Tong, X., Avallone, A., McCloskey, J., et al. (2011). Limited overlap between the seismic gap and coseismic slip of the great 2010 Chile earthquake. *Nature Geoscience*, *4*(3), 173–177. https://doi.org/10.1038/ngeo1073

Macintyre, I. G. (1972). Submerged reefs of eastern Caribbean. *AAPG Bulletin*, *56*(4), 720–738. https://doi.org/10.1306/819a407c-16c5-11d7-8645000102c1865d

Manaker, D. M., Calais, E., Freed, A. M., Ali, S. T., Przybylski, P., Mattioli, G., et al. (2008). Interseismic plate coupling and strain partitioning in the northeastern Caribbean. *Geophysical Journal International*, *174*(3), 889–903. https://doi.org/10.1111/j.1365-246x.2008.03819.x

McCann, W. R., & Sykes, L. R. (1984). Subduction of aseismic ridges beneath the Caribbean plate: Implications for the tectonics and seismic potential of the northeastern Caribbean. *Journal of Geophysical Research*, *89*(B6), 4493–4519. https://doi.org/10.1029/jb089ib06p04493

McHugh, C. M., Kanamatsu, T., Seeber, L., Bopp, R., Cormier, M.-H., & Usami, K. (2016). Remobilization of surficial slope sediment triggered by the A.D. 2011 M w 9 Tohoku-Oki earthquake and tsunami along the Japan Trench. *Geology*, *44*(5), 391–394. https://doi.org/10.1130/g37650.1

McHugh, C. M., Seeber, L., Braudy, N., Cormier, M.-H., Davis, M. B., Diebold, J. B., et al. (2011). Offshore sedimentary effects of the 12 January 2010 Haiti earthquake. *Geology*, *39*(8), 723–726. https://doi.org/10.1130/g31815.1

McHugh, C. M., Seeber, L., Rasbury, T., Strasser, M., Kioka, A., Kanamatsu, T., et al. (2020). Isotopic and sedimentary signature of megathrust ruptures along the Japan subduction margin. *Marine Geology*, *428*, 106283. https://doi.org/10.1016/j.margeo.2020.106283

Meltzner, A. J., Sieh, K., Chiang, H.-W., Shen, C.-C., Suwargadi, B. W., Natawidjaja, D. H., et al. (2012). Persistent termini of 2004-and 2005-like ruptures of the Sunda megathrust. *Journal of Geophysical Research*, *117*(B4), B04405. https://doi.org/10.1029/2011jb008888

Migeon, S., Garibaldi, C., Ratzov, G., Schmidt, S., Collot, J. Y., Zaragosi, S., & Texier, L. (2017). Earthquake-triggered deposits in the subduction trench of the north Ecuador/south Colombia margin and their implication for paleoseismology. *Marine Geology*, *384*, 47–62. https://doi.org/10.1016/j.margeo.2016.09.008

Minoura, K., Imamura, F., Sugawara, D., Kono, Y., & Iwashita, T. (2001). The 869 Jogan tsunami deposit and recurrence interval of large-scale tsunami on the Pacific coast of northeast Japan. *Journal of Natural Disaster Science*, *23*(2), 83–88.

Moernaut, J., Van Daele, M., Strasser, M., Clare, M. A., Heirman, K., Viel, M., et al. (2017). Lacustrine turbidites produced by surficial slope sediment remobilization: A mechanism for continuous and sensitive turbidite paleoseismic records. *Marine Geology*, *384*, 159–176. https://doi.org/10.1016/j.margeo.2015.10.009

Molenaar, A., Moernaut, J., Wiemer, G., Dubois, N., & Strasser, M. (2019). Earthquake impact on active margins: Tracing surficial remobilization and seismic strengthening in a slope sedimentary sequence. *Geophysical Research Letters*, *46*(11), 6015–6023. https://doi.org/10.1029/2019gl082350

Morena (2020). Paléosismologie et potentiel sismogène de la zone de subduction des petites Antilles à partir de l'enregistrement sédimentaire. PhD thesis. Université de Bretagne occidentale, ED n°598.

Morena, P., Ratzov, G., Cattaneo, A., Klingelhoefer, F., Beck, C., Seibert, C., et al. (2022). Coexistence of adjacent siliciclastic, carbonate, and mixed sedimentary systems: An example from seafloor morphology in the northern Lesser Antilles forearc. *Frontiers in Earth Science*, *10*, 834029. https://doi.org/10.3389/feart.2022.834029

Moreno, M., Rosenau, M., & Oncken, O. (2010). 2010 Maule earthquake slip correlates with pre-seismic locking of Andean subduction zone. *Nature*, *467*(7312), 198–202. https://doi.org/10.1038/nature09349

Mountjoy, J. J., Howarth, J. D., Orpin, A. R., Barnes, P. M., Bowden, D. A., Rowden, A. A., et al. (2018). Earthquakes drive large-scale submarine canyon development and sediment supply to deep-ocean basins. *Science Advances*, *4*(3), eaar3748. https://doi.org/10.1126/sciadv.aar3748

Mulder, T., Zaragosi, S., Razin, P., Grelaud, C., Lanfumey, V., & Bavoil, F. (2009). A new conceptual model for the deposition process of homogenite: Application to a cretaceous megaturbidite of the western Pyrenees (Basque region, SW France). *Sedimentary Geology*, *222*(3–4), 263–273. https://doi.org/10.1016/j.sedgeo.2009.09.013

Nakajima, T., & Kanai, Y. (2000). Sedimentary features of seismoturbidites triggered by the 1983 and older historical earthquakes in the eastern margin of the Japan Sea. *Sedimentary Geology*, *135*(1–4), 1–19. https://doi.org/10.1016/s0037-0738(00)00059-2

Noda, A., TuZino, T., Kanai, Y., Furukawa, R., & Uchida, J. (2008). Paleoseismicity along the southern Kuril Trench deduced from submarine-fan turbidites. *Marine Geology*, *254*(1–2), 73–90. https://doi.org/10.1016/j.margeo.2008.05.015

Normark, W. R., & Piper, D. J. (1991). Initiation processes and flow evolution of turbidity currents: Implications for the depositional record.

Ozawa, S., Nishimura, T., Suito, H., Kobayashi, T., Tobita, M., & Imakiire, T. (2011). Coseismic and postseismic slip of the 2011 magnitude-9 Tohoku-Oki earthquake. *Nature*, *475*(7356), 373–376. https://doi.org/10.1038/nature10227

Paterne, M., Feuillet, N., Cabioch, G., Cortijo, E., Blamart, D., Weill-Accardo, J., et al. (2018). Reservoir ages in the western tropical North Atlantic from one coral off Martinique Island (Lesser Antilles). *Radiocarbon*, *60*(2), 639–652. https://doi.org/10.1017/rdc.2017.118

Patton, J. R., Goldfinger, C., Morey, A. E., Ikehara, K., Romsos, C., Stoner, J., et al. (2015). A 6600 year earthquake history in the region of the 2004 Sumatra-Andaman subduction zone earthquake. *Geosphere*, *11*(6), 2067–2129. https://doi.org/10.1130/ges01066.1

Patton, J. R., Goldfinger, C., Morey, A. E., Romsos, C., Black, B., Djadjadihardja, Y., & Udrekh (2013). Seismoturbidite record as preserved at core sites at the Cascadia and Sumatra–Andaman subduction zones. *Natural Hazards and Earth System Sciences*, *13*(4), 833–867. https://doi.org/10.5194/nhess-13-833-2013

Philibosian, B., Feuillet, N., Weil-Accardo, J., Jacques, E., Guihou, A., Mériaux, A. S., et al. (2022). 20th-century strain accumulation on the Lesser Antilles megathrust based on coral microatolls. *Earth and Planetary Science Letters*, *579*, 117343. https://doi.org/10.1016/j.epsl.2021.117343

Philibosian, B., & Meltzner, A. J. (2020). Segmentation and supercycles: A catalog of earthquake rupture patterns from the Sumatran Sunda Megathrust and other well-studied faults worldwide. *Quaternary Science Reviews*, *241*, 106390. https://doi.org/10.1016/j.quascirev.2020.106390

Picard, M., Schneider, J.-L., & Boudon, G. (2006). Contrasting sedimentary processes along a convergent margin: The Lesser Antilles arc system. *Geo-Marine Letters*, *26*(6), 397–410. https://doi.org/10.1007/s00367-006-0046-y

Pichot, T., Patriat, M., Westbrook, G. K., Nalpas, T., Gutscher, M. A., Roest, W. R., et al. (2012). The Cenozoic tectonostratigraphic evolution of the Barracuda Ridge and Tiburon Rise, at the western end of the North America–South America plate boundary zone. *Marine Geology*, *303–306*, 154–171. https://doi.org/10.1016/j.margeo.2012.02.001

Pouderoux, H., Lamarche, G., & Proust, J.-N. (2012). Building an 18,000-year-long paleo-earthquake record from detailed deep-sea turbidite characterisation in Poverty Bay, New Zealand. *Natural Hazards and Earth System Sciences*, *12*(6), 2077–2101. https://doi.org/10.5194/nhess-12-2077-2012

Pouderoux, H., Proust, J.-N., & Lamarche, G. (2014). Submarine paleoseismology of the northern Hikurangi subduction margin of New Zealand as deduced from Turbidite record since 16 ka. *Quaternary Science Reviews*, *84*, 116–131. https://doi.org/10.1016/j.quascirev.2013.11.015

Prell, W. L., & Damuth, J. E. (1978). The climate-related diachronous disappearance of Pulleniatina obliquiloculata in late quaternary sediments of the Atlantic and Caribbean. *Marine Micropaleontology*, *3*, 267–277. https://doi.org/10.1016/0377-8398(78)90031-2

Puig, P., Ogston, A. S., Mullenbach, B. L., Nittrouer, C. A., Parsons, J. D., & Sternberg, R. W. (2004). Storminduced sediment gravity flows at the head of the Eel submarine canyon, northern California margin. *Journal of Geophysical Research*, *109*(C3), C03019. https://doi.org/10.1029/2003jc001918

Rama-Corredor, O., Martrat, B., Grimalt, J. O., López-Otalvaro, G. E., Flores, J. A., & Sierro, F. (2015). Parallelisms between sea surface temperature changes in the western tropical Atlantic (Guiana Basin) and high latitude climate signals over the last 140 000 years. *Climate of the Past*, *11*(10), 1297–1311. https://doi.org/10.5194/cp-11-1297-2015

Ratzov, G., Cattaneo, A., Babonneau, N., Deverchere, J., Yelles, K., Bracene, R., & Courboulex, F. (2015). Holocene turbidites record earthquake supercycles at a slow-rate plate boundary. *Geology*, *43*(4), 331–334. https://doi.org/10.1130/g36170.1

Reid, R. P., Carey, S. N., & Ross, D. R. (1996). Late Quaternary sedimentation in the Lesser Antilles island arc. *Geological Society of America Bulletin*, *108*(1), 78–100. https://doi.org/10.1130/0016-7606(1996)108<0078:lqsitl>2.3.co;2

Robson, G. R. (1964). An earthquake catalogue for the eastern Caribbean. *Bulletin of the Seismological Society of America*, *54*(2), 785–832. https://doi.org/10.1785/bssa0540020785

Ruiz, M., Galve, A., Monfret, T., Sapin, M., Charvis, P., Laigle, M., et al. (2013). Seismic activity offshore Martinique and Dominica islands (Central Lesser Antilles subduction zone) from temporary onshore and offshore seismic networks. *Tectonophysics*, *603*, 68–78. https://doi.org/10.1016/j.tecto.2011.08.006

Sainte-Claire Deville, C. (1843). *Observations sur le tremblement de terre éprouvé à la Guadeloupe le Février 1843*. Imprimerie du Gouverneur.

Seibert, C., Feuillet, N., Ratzov, G., Beck, C., & Cattaneo, A. (2020). Seafloor morphology and sediment transfer in the mixed carbonate-siliciclastic environment of the Lesser Antilles forearc along Barbuda to St. Lucia. *Marine Geology*, *428*, 106242. https://doi.org/10.1016/j.margeo.2020.106242

Seibert, C., Feuillet, N., Ratzov, G., Cattaneo, A., St-Onge, G., & Moreno, E. (2023a). Sedimentary cores CAS16-03PC and CAS16-14PC dataset from CASEIS Cruise [Dataset]. SEANOE. https://doi.org/10.17882/97660

Seibert, C., Feuillet, N., Ratzov, G., Cattaneo, A., St-Onge, G., & Moreno, E. (2023b). Sedimentary core CAS16-31PC dataset from CASEIS Cruise [Dataset]. SEANOE. https://doi.org/10.17882/97662

Seibert, C., Feuillet, N., Ratzov, G., Cattaneo, A., St-Onge, G., & Moreno, E. (2023c). Sedimentary core CAS16-06PC dataset from CASEIS Cruise [Dataset]. SEANOE. https://doi.org/10.17882/97657

Seibert, C., Feuillet, N., Ratzov, G., Cattaneo, A., St-Onge, G., & Moreno, E. (2023d). Sedimentary core CAS16-04PC dataset from CASEIS Cruise [Dataset]. SEANOE. https://doi.org/10.17882/97656

Seibert, C., Feuillet, N., Ratzov, G., Cattaneo, A., St-Onge, G., & Moreno, E. (2023e). Sedimentary core CAS16-07PC dataset from CASEIS Cruise [Dataset]. SEANOE. https://doi.org/10.17882/97658

Seibert, C., Feuillet, N., Ratzov, G., Cattaneo, A., St-Onge, G., & Moreno, E. (2023f). Sedimentary core CAS16-01PC dataset from CASEIS Cruise [Dataset]. SEANOE. https://doi.org/10.17882/97033

Shepherd, J. B. (1992). Comment on "subduction and seismic hazard in the Lesser Antilles" by Pascal Bernard and Jérôme Lambert. *Bulletin of the Seismological Society of America*, *82*(3), 1534–1543. https://doi.org/10.1785/bssa0820031534

Sieh, K., Natawidjaja, D. H., Meltzner, A. J., Shen, C. C., Cheng, H., Li, K. S., et al. (2008). Earthquake supercycles inferred from sea-level changes recorded in the corals of west Sumatra. *Science*, *322*(5908), 1674–1678. https://doi.org/10.1126/science.1163589

Stein, S., Engeln, J. F., Wiens, D. A., Fujita, K., & Speed, R. C. (1982). Subduction seismicity and tectonics in the Lesser Antilles arc. *Journal of Geophysical Research*, *87*(B10), 8642–8664. https://doi.org/10.1029/jb087ib10p08642

Stevens, T., Paull, C. K., Ussler, W., III, McGann, M., Buylaert, J. P., & Lundsten, E. (2014). The timing of sediment transport down Monterey Submarine Canyon, offshore California. *Bulletin*, *126*(1–2), 103–121. https://doi.org/10.1130/b30931.1

Stuiver, M., Reimer, P. J., & Reimer, R. W. (2021). CALIB 8.2 [WWW program]. Retrieved from http://calib.org

Sykes, L. R., & Ewing, M. (1965). The seismicity of the Caribbean region. *Journal of Geophysical Research*, *70*(20), 5065–5074. https://doi.org/10.1029/jz070i020p05065

Symithe, S., Calais, E., de Chabalier, J. B., Robertson, R., & Higgins, M. (2015). Current block motions and strain accumulation on active faults in the Caribbean. *Journal of Geophysical Research: Solid Earth*, *120*(5), 3748–3774. https://doi.org/10.1002/2014jb011779

Talling, P. J. (2014). On the triggers, resulting flow types and frequencies of subaqueous sediment density flows in different settings. *Marine Geology*, *352*, 155–182. https://doi.org/10.1016/j.margeo.2014.02.006

Tong, X., Sandwell, D., Luttrell, K., Brooks, B., Bevis, M., Shimada, M., et al. (2010). The 2010 Maule, Chile earthquake: Downdip rupture limit revealed by space geodesy. *Geophysical Research Letters*, *37*(24), L24311. https://doi.org/10.1029/2010gl045805

Trofimovs, J., Talling, P. J., Fisher, J. K., Sparks, R. S. J., Watt, S. F. L., Hart, M. B., et al. (2013). Timing, origin and emplacement dynamics of mass flows offshore of SE Montserrat in the last 110 ka: Implications for landslide and tsunami hazards, eruption history, and volcanic island evolution: Mass flows offshore of Montserrat. *Geochemistry, Geophysics, Geosystems*, *14*(2), 385–406. https://doi.org/10.1002/ggge.20052

Usami, K., Ikehara, K., Kanamatsu, T., & McHugh, C. M. (2018). Supercycle in great earthquake recurrence along the Japan Trench over the last 4000 years. *Geoscience Letters*, *5*(1), 11. https://doi.org/10.1186/s40562-018-0110-2

Van Daele, M., Araya-Cornejo, C., Pille, T., Vanneste, K., Moernaut, J., Schmidt, S., et al. (2019). Distinguishing intraplate from megathrust earthquakes using lacustrine turbidites. *Geology*, *47*(2), 127–130. https://doi.org/10.1130/g45662.1

Van Daele, M., Meyer, I., Moernaut, J., De Decker, S., Verschuren, D., & De Batist, M. (2017). A revised classification and terminology for stacked and amalgamated turbidites in environments dominated by (hemi)pelagic sedimentation. *Sedimentary Geology*, *357*, 72–82. https://doi.org/10.1016/j.sedgeo.2017.06.007

van Rijsingen, E., Calais, E., Jolivet, R., de Chabalier, J. B., Robertson, R., Ryan, G. A., & Symithe, S. (2021). Vertical tectonic motions in the Lesser Antilles: Linking short-and long-term observations.

van Rijsingen, E., Lallemand, S., Peyret, M., Arcay, D., Heuret, A., Funiciello, F., & Corbi, F. (2018). How subduction interface roughness influences the occurrence of large interplate earthquakes. *Geochemistry, Geophysics, Geosystems*, *19*(8), 2342–2370. https://doi.org/10.1029/2018gc007618

Vermassen, F., Van Daele, M., Praet, N., Cnudde, V., Kissel, C., & Anselmetti, F. S. (2023). Unravelling megaturbidite deposition: Evidence for turbidite stacking/amalgamation and seiche influence during the 1601 CE earthquake at Lake Lucerne, Switzerland. *Sedimentology*, *70*(5), 1496–1520. https://doi.org/10.1111/sed.13094

Vigny, C., Socquet, A., Peyrat, S., Ruegg, J. C., Métois, M., Madariaga, R., et al. (2011). The 2010 M w 8.8 Maule megathrust earthquake of central Chile, monitored by GPS. *Science*, *332*(6036), 1417–1421. https://doi.org/10.1126/science.1204132

Wallace, L. M., Ellis, S., Miyao, K., Miura, S., Beavan, J., & Goto, J. (2009). Enigmatic, highly active left-lateral shear zone in southwest Japan explained by aseismic ridge collision. *Geology*, *37*(2), 143–146. https://doi.org/10.1130/g25221a.1

Wang, K., & Bilek, S. L. (2014). Invited review paper: Fault creep caused by subduction of rough seafloor relief. *Tectonophysics*, *610*, 1–24. https://doi.org/10.1016/j.tecto.2013.11.024

Wang, Y. C., Gieskes, J. M., & Musoke, L. (1990). Bulk chemical analysis of sediments-Hole 671B. In J. C. Moore, A. Mascle, E. Taylor, P. D. Rabinowitz, A. W. Meyer, & L. E. Garrison (Eds.), *Proceeding of the ocean drilling program, scientific results* (Vol. 110, pp. 179–188).

Weil-Accardo, J., Feuillet, N., Jacques, E., Deschamps, P., Beauducel, F., Cabioch, G., et al. (2016). Two hundred thirty years of relative sea level changes due to climate and megathrust tectonics recorded in coral microatolls of Martinique (French West Indies). *Journal of Geophysical Research: Solid Earth*, *121*(4), 2015JB012406. https://doi.org/10.1002/2015jb012406

Wells, D. L., & Coppersmith, K. J. (1994). New empirical relationships among magnitude, rupture length, rupture width, rupture area, and surface displacement. *Bulletin of the Seismological Society of America*, *84*(4), 974–1002. https://doi.org/10.1785/bssa0840040974

Wils, K., Deprez, M., Kissel, C., Vervoort, M., Van Daele, M., Daryono, M. R., et al. (2021). Earthquake doublet revealed by multiple pulses in lacustrine seismo-turbidites. *Geology*, *49*(11), 1301–1306. https://doi.org/10.1130/g48940.1

Wils, K., Van Daele, M., Kissel, C., Moernaut, J., Schmidt, S., Siani, G., & Lastras, G. (2020). Seismo-turbidites in Aysén Fjord (southern Chile) reveal a complex pattern of rupture modes along the 1960 megathrust earthquake segment. *Journal of Geophysical Research: Solid Earth*, *125*(9), e2020JB019405. https://doi.org/10.1029/2020jb019405

Wilson, B. (2008). Late Quaternary benthonic foraminifera in a bathyal core from the Leeward Islands, Lesser Antilles, NE Caribbean Sea. *Journal of Micropalaeontology*, *27*(2), 177–188. https://doi.org/10.1144/jm.27.2.177

Woerther, P. (2016). *ESS_K-16-ATA cruise*. RV L'Atalante. https://doi.org/10.17600/16000300